

# NLO QCD corrections to full off-shell production of $t\bar{t}Z$ including leptonic decays

Giuseppe Bevilacqua,<sup>a</sup> Heribertus Bayu Hartanto,<sup>b</sup> Manfred Kraus,<sup>c</sup> Jasmina Nasufi<sup>d</sup> and Malgorzata Worek<sup>d</sup>

<sup>a</sup>*ELKH-DE Particle Physics Research Group, University of Debrecen, H-4010 Debrecen, P.O. Box 105, Hungary*

<sup>b</sup>*Cavendish Laboratory, University of Cambridge, Cambridge CB3 0HE, United Kingdom*

<sup>c</sup>*Physics Department, Florida State University, Tallahassee, FL 32306-4350, USA*

<sup>d</sup>*Institute for Theoretical Particle Physics and Cosmology, RWTH Aachen University, D-52056 Aachen, Germany*

*E-mail:* [giuseppe.bevilacqua@science.unideb.hu](mailto:giuseppe.bevilacqua@science.unideb.hu), [hbhartanto@hep.phy.cam.ac.uk](mailto:hbhartanto@hep.phy.cam.ac.uk), [mkraus@hep.fsu.edu](mailto:mkraus@hep.fsu.edu), [jasmina.nasufi@rwth-aachen.de](mailto:jasmina.nasufi@rwth-aachen.de), [worek@physik.rwth-aachen.de](mailto:worek@physik.rwth-aachen.de)

**ABSTRACT:** Motivated by ongoing new physics searches in the top-quark sector at the Large Hadron Collider we report on the calculation of NLO QCD corrections to the Standard Model  $pp \rightarrow t\bar{t}Z + X$  process in the tetra-lepton decay channel. This calculation is based on the matrix elements for the  $e^+\nu_e\mu^-\bar{\nu}_\mu b\bar{b}\tau^+\tau^-$  final state and includes all resonant and non-resonant Feynman diagrams, interferences and off-shell effects of the top quark as well as the  $W$  and  $Z$  gauge bosons. Also incorporated are photon-induced contributions. As it is customary for such studies, we show theoretical predictions for both fixed and dynamical factorisation and renormalisation scale choices and different PDF sets. Furthermore, we study the main theoretical uncertainties that are associated with neglected higher-order terms in the perturbative expansion and with the parameterisation of the PDF sets. In order to investigate the size of off-shell effects and higher-order corrections in top-quark decays, we perform a second computation for this process, which is based on the narrow-width-approximation where the top quarks,  $W$  and  $Z$  gauge bosons are kept on-shell. Results are given for the integrated and differential fiducial cross sections for the LHC Run II center-of-mass energy of 13 TeV.

**KEYWORDS:** Higher-Order Perturbative Calculations, Top Quark

TTK-22-02, P3H-22-002, CAVENDISH-HEP-22/03

---

## Contents

<b>1</b>	<b>Introduction</b>	<b>1</b>
<b>2</b>	<b>Details of the calculation</b>	<b>3</b>
<b>3</b>	<b>Computational setup</b>	<b>7</b>
<b>4</b>	<b>Integrated fiducial cross sections</b>	<b>8</b>
<b>5</b>	<b>Differential fiducial cross sections</b>	<b>15</b>
<b>6</b>	<b>Off-shell vs on-shell modelling of top quarks and gauge bosons</b>	<b>19</b>
<b>7</b>	<b>Summary</b>	<b>27</b>

---

## 1 Introduction

The frontier center-of-mass energy and the ever-increasing luminosity of proton collisions at the Large Hadron Collider (LHC) enable precise studies of Standard Model (SM) processes with small production rates, such as the associated production of a  $t\bar{t}$  pair and a  $Z$  boson. Among various possible decay channels for this process the final state containing four charged leptons (electrons or muons) is the cleanest from the experimental point of view and the most interesting for theoretical studies. This channel is often referred to as the tetra-lepton channel and abbreviated as  $4\ell$ . Indeed, the measurements of the charged multi-lepton final states are particularly precise at the LHC due to the excellent lepton identification and selection in the ATLAS and CMS detectors. In fact, both ATLAS and CMS collaborations have already used events with four charged leptons and measured the inclusive cross section for  $t\bar{t}Z$  production [1, 2]. In addition, the differential cross section was measured as a function of a few observables [3, 4]. Processing the full Run II data ( $\mathcal{L} = 139 \text{ fb}^{-1}$ ), fairly good agreement between data and theoretical predictions at the differential level has been found. Interestingly, observables directly connected to the  $Z$  boson show poorer agreement. The upcoming LHC Run 3 and the future high-luminosity LHC upgrade would definitely require more accurate modelling of production and decays for the  $t\bar{t}Z$  process. A good theoretical knowledge of the  $t\bar{t}Z$  process is needed not only for an accurate prediction of fiducial cross section and better understanding of the various properties of the top quark, but it is also a fundamental prerequisite for the correct interpretation of possible new physics signals that may arise in this channel. The  $t\bar{t}Z$  production process provides direct access to the coupling of the top quark to the neutral electroweak gauge bosons. It gives important insights into the top quark, that are complementary to  $t\bar{t}$  and single top quark production as well as to the  $t \rightarrow Wb$  decay. Any deviations of the coupling strength of the top quark to the  $Z$  boson from its SM value might imply the existence of new physics effects. In particular, the  $t\bar{t}Z$  coupling might be affected by a tree-level mixing with additional  $Z'$  gauge bosons and vector-like leptons, see e.g. [5–11]. Such deviations can be probed for example in the context of effective field theory [12–24]. Additionally,  $t\bar{t}Z$  production is among the most important background processes for several new physics scenarios. They comprise final states with multiple charged leptons, missing transverse momentum and  $b$ -jets and are

vigorously searched for at the LHC [25–30]. Finally, the  $t\bar{t}Z$  process plays a very prominent role in studies of important SM processes. Here, good examples comprise  $t\bar{t}$  production in association with a Higgs boson [31–33] and single top quark production in association with a  $Z$  boson [34, 35]. Therefore, providing a reliable and accurate description of  $pp \rightarrow t\bar{t}Z$  production to advance our understanding of the process and to facilitate comparisons with constantly increasing and improving LHC data, is more timely than ever. To improve our understanding of  $t\bar{t}Z$  various effects must be considered and taken into account already at the matrix element level, omitting, as much as possible, approximations when incorporating them. One might expect to at least examine where the approximations used may fail. Furthermore, it might not be sufficient to incorporate various effects, such as spin-correlated decays, at the lowest order in the perturbative expansion. Indeed, higher-order corrections not only induce substantial normalisation and shape differences but also strongly reduce systematical uncertainties associated with theoretical predictions. So it is necessary to include next-to-leading order (NLO) QCD and electroweak corrections wherever possible to claim high-precision predictions for  $pp \rightarrow t\bar{t}Z$ .

For the inclusive  $t\bar{t}Z$  production, with stable top quarks and an on-shell  $Z$  gauge boson, NLO QCD corrections have been around for over ten years [36]. They have been afterwards recomputed in Refs. [37, 38]. Furthermore, results with NLO electroweak (EW) corrections have been provided in the literature [39]. Besides NLO QCD and EW corrections, a further step towards a more precise modelling of the  $t\bar{t}Z$  production process has been achieved by including soft gluon resummation effects at next-to-next-to-leading logarithmic accuracy [40–43]. The calculations mentioned above provide important information about the impact of higher-order corrections to the total  $t\bar{t}Z$  production rate. However, since decays of unstable top quarks and  $Z$  bosons are not taken into account, they are neither capable to ensure a reliable description of the fiducial phase space regions nor can they give us a glimpse into the top quark radiation pattern. Thus, for more realistic studies the decays of unstable particles must be taken into account. For the latter various modelling approaches are available in the literature. Firstly, NLO QCD theoretical predictions for stable top quarks and a  $Z$  boson have been matched with parton shower (PS) Monte Carlo (MC) programs [44, 45]. In this case top quark and  $Z$  gauge boson decays have been treated in the parton shower approximation omitting spin correlations even at leading order. Very recently, improved NLO + PS predictions for  $t\bar{t}Z$  have been provided [46]. Specifically, the  $pp \rightarrow t\bar{t}\ell^+\ell^-$  process with  $\ell$  denoting either  $e^\pm$  or  $\mu^\mp$  have been matched to PS programs including both resonant and non-resonant  $Z$ - as well as photon-induced contributions. Furthermore, decays of the top quarks with full tree-level spin correlations in the narrow-width-approximation (NWA) have been taken into account according to the method proposed in Ref. [47]. A different approach has been considered in Ref. [15], where both top quark and  $Z$  gauge boson are treated in NWA, but NLO QCD corrections in both production and decay stages are taken into account. In this way, contributions which are parametrically suppressed by  $\mathcal{O}(\Gamma/m)$ , arising from off-shell top quarks or  $W/Z$  bosons, have been neglected. Also the contribution from the  $t \rightarrow WbZ$  decay has been neglected due to the tiny available phase space and the size of the  $t \rightarrow WbZ$  branching ratio. The latter is of the order of  $\mathcal{B}_{t \rightarrow WbZ} \approx 2 \times 10^{-6}$  for the top quark mass range  $m_t \in (170 - 180)$  GeV [48]. Finally, state-of-the-art NLO QCD predictions have been provided for the  $t\bar{t}Z$  process in the di-lepton top quark decay channel [49]. More precisely, NLO QCD corrections to the  $pp \rightarrow e^+\nu_e\mu^-\nu_\mu\bar{b}\bar{b}\nu_\tau\bar{\nu}_\tau + X$  final state have been calculated. All double-, single- and non-resonant Feynman diagrams, interferences, and off-shell effects of the top quarks have been properly incorporated at NLO QCD. Non-resonant and off-shell effects due to the finite  $W$ - and  $Z$ -boson width have been included as well. Furthermore, full off-shell  $t\bar{t}Z$  predictions at NLO in QCD have been compared to those computed in the NWA approach [50]. Similar studies for the production of  $t\bar{t}Z$  with the  $Z$  boson decaying into charged leptons, however, are still

missing.

The purpose of this article is to mitigate this situation and to calculate for the first time NLO QCD corrections to the  $e^+\nu_e\mu^-\bar{\nu}_\mu b\bar{b}\tau^+\tau^-$  final state for the LHC Run II center-of-mass system energy of  $\sqrt{s} = 13$  TeV. We only simulate decays of the weak bosons to different lepton generations, however, these interference effects are at the per-mille level for inclusive cuts. Thus, the complete  $pp \rightarrow \ell^+\nu_\ell\ell^-\bar{\nu}_\ell b\bar{b}\ell^+\ell^- + X$  cross section (with  $\ell = e^\pm, \mu^\pm$ ) can be obtained by multiplying the results from this paper with a lepton-flavour factor of 8. Our calculations comprise all quantum effects at the matrix element level. We scrutinise the size of higher-order corrections and theoretical uncertainties in such a complex environment. We additionally address the choice of a judicious renormalisation and factorisation scale setting. Afterwards, the size of off-shell effects of the top quarks and gauge bosons is examined at the integrated and differential level. The latter study is carried out with the help of a second computation that we perform for this process based on the NWA approach. Specifically, we compare results from the full off-shell calculation against predictions based on the full NWA as well as on the NWA with leading order (LO) top-quark decays (abbreviated as  $\text{NWA}_{\text{LOdec}}$ ). By employing  $\text{NWA}_{\text{LOdec}}$  results, we are able to estimate the size of the NLO QCD corrections to top quark decays. It should be clear that, in the full off-shell picture, the contribution of the  $Z \rightarrow \tau^+\tau^-$  decay must be complemented by its photon-induced counterpart,  $\gamma^* \rightarrow \tau^+\tau^-$ , in order to preserve gauge invariance. Therefore, like Ref. [46], we are in the condition of examining more realistically the impact of photon contributions and in particular of the  $Z/\gamma^*$  interference on integrated and differential fiducial cross sections. Finally, the effect of applying an additional cut on the invariant mass of the  $\tau$  lepton pair is studied. In particular, we investigate the requirement that the invariant mass of the  $\tau$  leptons is set in a specific mass window around the  $Z$  boson mass.

The paper is organised as follows. In Section 2 we briefly summarise the framework of our calculation and discuss technical aspects of the computation. We outline the theoretical setup for LO and NLO QCD results in Section 3. Results for the integrated fiducial cross sections are presented in Section 4. They are provided for the LHC center-of-mass system energy of 13 TeV and for a fixed and dynamical renormalisation and factorisation scale choice. In Section 5 predictions for a few differential fiducial cross sections are given. Additionally, theoretical uncertainties associated with the neglected higher order terms in the perturbative expansion and different parameterisations of the parton distribution functions are discussed in Sections 4 and 5. Theoretical predictions for  $t\bar{t}Z$  in the NWA are provided in Section 6. Also there the size of off-shell effects is examined together with the impact of higher-order corrections to top-quark decays. Finally, we summarise the results and outline our conclusions in Section 7.

## 2 Details of the calculation

In  $pp$  collisions at the LHC the  $e^+\nu_e\mu^-\bar{\nu}_\mu b\bar{b}\tau^+\tau^-$  final state is produced via the scattering of two gluons or a  $q\bar{q}$  pair, where  $q$  stands for up- or down-type quarks. The contributions to the tree-level squared amplitude at  $\mathcal{O}(\alpha_s^2\alpha^6)$  can be subdivided into three classes: diagrams containing two top-quark propagators that can become resonant, diagrams containing only one top-quark resonance and finally diagrams without any top-quark resonance. For the  $Z$  and  $W$  gauge bosons, resonant and non-resonant contributions are present. In the former case also photon-induced contributions and the  $Z/\gamma^*$  interference effects are included. Examples of Feynman diagrams are depicted in Figure 1. The FEYNGAME program [51] is employed to draw all Feynman diagrams in this article. In total, there are 1836 LO diagrams for the  $gg \rightarrow e^+\nu_e\mu^-\bar{\nu}_\mu b\bar{b}\tau^+\tau^-$  partonic reaction and 980 diagrams for each  $q\bar{q} \rightarrow e^+\nu_e\mu^-\bar{\nu}_\mu b\bar{b}\tau^+\tau^-$  subprocess. Even though we do not employ Feynman diagrams in our

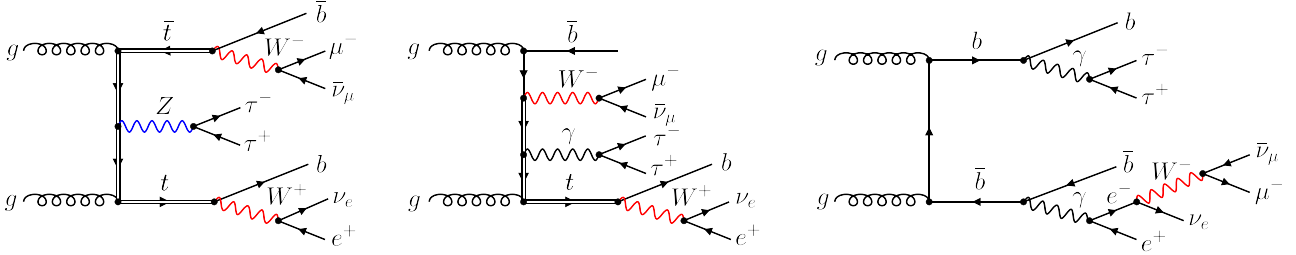


**Figure 1.** Representative Feynman diagrams with double- (left), single- (middle) and no top-quark resonances (right) contributing to the  $gg \rightarrow e^+ \nu_e \mu^- \bar{\nu}_\mu b \bar{b} \tau^+ \tau^-$  partonic subprocess at leading order. The middle and right diagram comprise no  $Z$  resonances whereas the third one involves only a single  $W$  boson. They contribute to  $Z$  and  $W$  off-shell effects.

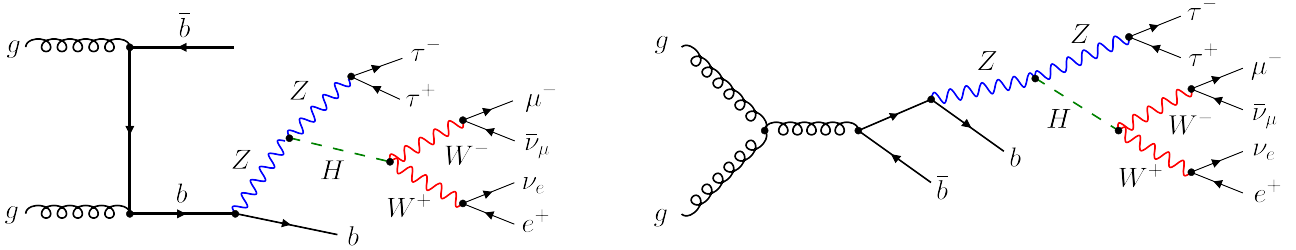


**Figure 2.** Representative Feynman diagrams with the Higgs-boson-exchange contribution that appear in the  $gg \rightarrow e^+ \nu_e \mu^- \bar{\nu}_\mu b \bar{b} \tau^+ \tau^-$  partonic subprocess at leading order even though the  $b$  quarks and  $\tau^\pm$  leptons are treated as massless particles.

calculations we present their numbers as a measure of the complexity of the calculation. Let us note that, even in the case where  $b$  quarks and  $\tau$  leptons are treated as massless particles, a number of Higgs-boson exchange diagrams contribute to the amplitude. Specifically, there are 1844 diagrams for the  $gg$  initiated subprocess that need to be considered if the Higgs boson is included and 984 for each  $q\bar{q}$  channel. Examples of the corresponding Feynman diagrams for the  $gg \rightarrow e^+ \nu_e \mu^- \bar{\nu}_\mu b \bar{b} \tau^+ \tau^-$  partonic reaction are depicted in Figure 2. The Higgs boson contribution, however, is well below 0.1% level as we have checked by an explicit LO calculation using  $m_H = 125$  GeV and  $\Gamma_H = 4.07 \times 10^{-3}$  GeV. Thus, it is neglected throughout our calculations. Furthermore, LO contributions induced by the bottom-quark parton density are at the permille level, i.e. they are of the order of 0.3%. Also these contributions are not taken into account in our study.

The calculation of LO contributions is performed automatically with the help of the HELAC-DIPOLES package [52]. The results are cross checked with the HELAC-PHEGAS program [53]. Both packages are based on the well-known off-shell iterative algorithm for scattering amplitudes [54–56]. The integration over the momentum fractions  $x_1, x_2$  of the initial-state partons is optimised with the help of PARNI [57]. The phase space integration is executed with the help of KALEU [58] and cross checked with PHEGAS [59]. The inclusion of the decays of top quarks,  $W^\pm$  and  $Z$  gauge bosons is performed in the complex mass scheme [60, 61]. Such a scheme fully respects gauge invariance and is straightforward to apply.

The virtual corrections consist of the 1-loop corrections to the LO contributions. For our process one can classify the corrections into self-energy, vertex, box-type, pentagon-type, hexagon-type and

ONE-LOOP CORRECTION	NUMBER OF FEYNMAN DIAGRAMS
SELF-ENERGY	32040
VERTEX	39288
BOX-TYPE	21452
PENTAGON-TYPE	8604
HEXAGON-TYPE	1996
HEPTAGON-TYPE	180
TOTAL NUMBER	103560

**Table 1.** Number of one-loop Feynman diagrams for the dominant  $gg \rightarrow e^+ \nu_e \mu^- \bar{\nu}_\mu \bar{b} \bar{b} \tau^+ \tau^-$  partonic subprocess at  $\mathcal{O}(\alpha_s^3 \alpha^6)$  for the  $pp \rightarrow e^+ \nu_e \mu^- \bar{\nu}_\mu \bar{b} \bar{b} \tau^+ \tau^- + X$  process. The Higgs boson exchange contributions are not considered and the Cabibbo-Kobayashi-Maskawa mixing matrix is kept diagonal.

heptagon-type topologies. In Table 1 the number of one-loop Feynman diagrams, that corresponds to each type of correction for the dominant  $gg \rightarrow e^+ \nu_e \mu^- \bar{\nu}_\mu \bar{b} \bar{b} \tau^+ \tau^-$  partonic subprocess as obtained with QGRAF [62], is given. In Table 2 similar results are displayed for the  $q\bar{q} \rightarrow e^+ \nu_e \mu^- \bar{\nu}_\mu \bar{b} \bar{b} \tau^+ \tau^-$  partonic subprocess. To evaluate the virtual corrections, HELAC-1LOOP [63] is used, which is based on the HELAC-PHEGAS program to calculate all tree-level like ingredients and the OPP reduction method [64]. The cut-constructible part of the virtual amplitudes as well as the rational term  $R_1$  of the amplitude is computed using the CUTTOOLS code [65, 66]. The  $R_2$  term, on the other hand, is obtained with the help of extra Feynman rules [67]. At the one-loop level the appearance of a non-zero top-quark width in the propagator requires the evaluation of scalar integrals with complex masses. For this task the program ONELOOP [68] is employed. We chose to renormalise the strong coupling in the  $\overline{\text{MS}}$  scheme with five active flavours and the top quark decoupled, while the mass renormalisation is performed in the on-shell scheme. The correctness of the calculation is checked by a series of tests performed both at the preparation stage and at runtime. We have checked that our one-loop amplitudes agree with the results of MADGRAPH5\_AMC@NLO [69] for a few phase space points and for both  $gg$  and  $q\bar{q}$  subprocesses. Additionally, the cancellation of the infrared  $1/\epsilon^2$  and  $1/\epsilon$  poles between virtual and real corrections, as provided by the  $\mathcal{I}$ -operator, has been checked numerically. We also monitor the numerical stability by checking Ward identities at every phase space point. The events which do not pass this runtime check are not discarded from the calculation of the finite part, but rather recalculated with higher precision. For the  $q\bar{q}$  subprocess we use the so-called scale test [70], which is based on momentum rescaling.

For the real corrections the generic subprocesses are listed in Table 3 where again  $q$  stands for up- or down-type quarks. All subprocesses include all possible contributions of the order of  $\mathcal{O}(\alpha_s^3 \alpha^6)$ . The complex mass scheme for unstable top quarks and gauge bosons has been implemented in complete analogy to the LO case. For the calculation of the real emission contributions, the HELAC-DIPOLES package is employed. It implements the Catani-Seymour dipole formalism [71, 72] for arbitrary helicity eigenstates and colour configurations of the external partons [52]. Furthermore, it comprises the Nagy-Soper subtraction scheme [73], which makes use of random polarisation and colour sampling of the external partons. In Table 3 we provide additionally the number of Catani-Seymour dipoles and Nagy-

ONE-LOOP CORRECTION	NUMBER OF FEYNMAN DIAGRAMS
SELF-ENERGY	18338
VERTEX	10272
BOX-TYPE	5218
PENTAGON-TYPE	1900
HEXAGON-TYPE	380
HEPTAGON-TYPE	32
TOTAL NUMBER	36140

**Table 2.** As in Table 1 but for the  $q\bar{q} \rightarrow e^+\nu_e\mu^-\bar{\nu}_\mu b\bar{b}\tau^+\tau^-$  partonic subprocess.

PARTONIC SUBPROCESS	NUMBER OF FEYNMAN DIAGRAMS	NUMBER OF CS DIPOLES	NUMBER OF NS SUBTRACTIONS
$gg \rightarrow e^+\nu_e\mu^-\bar{\nu}_\mu b\bar{b}\tau^+\tau^- g$	12378	27	9
$gq \rightarrow e^+\nu_e\mu^-\bar{\nu}_\mu b\bar{b}\tau^+\tau^- q$	6416	15	5
$g\bar{q} \rightarrow e^+\nu_e\mu^-\bar{\nu}_\mu b\bar{b}\tau^+\tau^- \bar{q}$	6416	15	5
$q\bar{q} \rightarrow e^+\nu_e\mu^-\bar{\nu}_\mu b\bar{b}\tau^+\tau^- g$	6416	15	5

**Table 3.** List of partonic subprocesses contributing to the subtracted real emission at  $\mathcal{O}(\alpha_s^3\alpha^6)$  for the  $pp \rightarrow e^+\nu_e\mu^-\bar{\nu}_\mu b\bar{b}\tau^+\tau^- + X$  process where  $q = u, d, c, s$ . Also shown are the number of Feynman diagrams, as well as the number of Catani-Seymour and Nagy-Soper subtraction terms that correspond to these partonic subprocesses.

Soper subtraction terms. Even though we employ the Nagy-Soper subtraction scheme for the full off-shell calculation, we show numbers for both schemes to underline the difference between them. Indeed, the difference between the number of Catani-Seymour dipoles and Nagy-Soper subtraction terms corresponds to the total number of possible spectators that are only relevant in the Catani-Seymour subtraction scheme. To check our calculation we have explored the independence of the real emission results on the unphysical cutoff in the dipole subtraction phase space, see e.g. [74–77].

The HELAC-1LOOP program and HELAC-DIPOLES are part of the HELAC-NLO framework [78]. Theoretical predictions obtained with the help of the HELAC-NLO software are stored in the form of modified Les Houches Event Files [79] and ROOT Ntuples [80]. Incorporating ideas outlined in Ref. [81] we store each “event” with supplementary matrix element and PDF information. This allows us to obtain results for different scale settings and PDF choices by reweighting. Furthermore, storing “events” has clear advantages when different observables and/or binning are needed, and when different, more exclusive, sets of selection cuts are to be used. Indeed, no additional time-consuming code running is required in such cases.

### 3 Computational setup

We consider the  $pp \rightarrow e^+ \nu_e \mu^- \bar{\nu}_\mu b \bar{b} \tau^+ \tau^- + X$  process at the LHC Run II center-of-mass energy of  $\sqrt{s} = 13$  TeV. Specifically, we calculate  $\alpha_s$  corrections to the born-level process at  $\mathcal{O}(\alpha_s^2 \alpha^6)$ . We only simulate decays of the weak bosons to different lepton generations. Interference effects related to same-flavor leptons, however, are at the permille level for inclusive cuts. We have checked this by an explicit leading-order calculation for the  $pp \rightarrow e^+ \nu_e e^- \bar{\nu}_e b \bar{b} e^+ e^- + X$ ,  $pp \rightarrow e^+ \nu_e \mu^- \bar{\nu}_\mu b \bar{b} e^+ e^- + X$  as well as  $pp \rightarrow e^+ \nu_e e^- \bar{\nu}_e b \bar{b} \tau^+ \tau^- + X$  process and found differences up to 0.2% only. In our calculations the Cabibbo-Kobayashi-Maskawa mixing matrix is kept diagonal. The unstable particles, top quarks,  $W$  and  $Z$  gauge bosons, are treated within the complex-mass scheme. The Higgs boson and initial state bottom quark contributions are neglected, as explained in the previous section. The Standard Model parameters are given within the  $G_\mu$  scheme

$$\begin{aligned}
G_\mu &= 1.16638 \cdot 10^{-5} \text{ GeV}^{-2}, & m_t &= 173 \text{ GeV}, \\
m_W &= 80.351972 \text{ GeV}, & \Gamma_W^{\text{NLO}} &= 2.0842989 \text{ GeV}, \\
m_Z &= 91.153481 \text{ GeV}, & \Gamma_Z^{\text{NLO}} &= 2.4942664 \text{ GeV}.
\end{aligned}
\tag{3.1}$$

All other particles, including bottom quarks and  $\tau$  leptons, are considered massless. The top-quark width is treated as a fixed parameter throughout this work and its value corresponds to a fixed scale  $\mu_R = m_t$  that is most natural for top-quark decays. The  $\alpha_s(m_t)$  parameter used in the calculation of  $\Gamma_t^{\text{NLO}}$  is independent of  $\alpha_s(\mu_0)$  that goes into the matrix element calculations as well as PDFs, since the latter describes the dynamics of the whole process. Computed for unstable  $W$  bosons while neglecting the bottom-quark mass the top-quark width reads

$$\Gamma_t^{\text{LO}} = 1.443303 \text{ GeV}, \quad \Gamma_t^{\text{NLO}} = 1.3444367445 \text{ GeV}.
\tag{3.2}$$

For the NWA case with on-shell  $W$  gauge boson, in the limit  $\Gamma_W/m_W \rightarrow 0$ , we obtain instead

$$\Gamma_{t,\text{NWA}}^{\text{LO}} = 1.466332 \text{ GeV}, \quad \Gamma_{t,\text{NWA}}^{\text{NLO}} = 1.365888 \text{ GeV}.
\tag{3.3}$$

The LO and NLO top-quark widths are computed using formulas from Refs. [82, 83]. All final-state  $b$  and light quarks as well as gluons with pseudorapidity  $|\eta| < 5$  are recombined into jets with the separation parameter  $R = 0.4$  in the rapidity-azimuthal angle plane via the IR-safe *anti- $k_T$*  jet clustering algorithm [84]. Moreover, we impose additional cuts on the transverse momenta and the rapidity of  $b$ -jets

$$p_{T,b} > 25 \text{ GeV}, \quad |y_b| < 2.5, \quad \Delta R_{bb} > 0.4,
\tag{3.4}$$

where  $b$  stands for the two  $b$ -jets. The following selection criteria are imposed to ensure that all charged leptons are observed inside the detector and are well separated from each other

$$p_{T,\ell} > 20 \text{ GeV}, \quad |y_\ell| < 2.5, \quad \Delta R_{\ell\ell} > 0.4,
\tag{3.5}$$

where  $\ell = e, \mu, \tau$ . The minimum on the missing transverse momentum from undetected neutrinos is set to be

$$p_T^{\text{miss}} > 40 \text{ GeV}.
\tag{3.6}$$

We set no restrictions on the kinematics of the extra light jet. We require 2  $b$ -jets, 4 charged leptons and missing transverse momentum. The applied cuts are motivated by recent experimental analyses

from ATLAS [4] and CMS [3]. Following the recommendations of PDF4LHC [85] we consistently use the NNPDF3.1 [86] sets of parton distribution functions. The two-loop (one-loop) running of  $\alpha_s$  at NLO (LO) is provided by the LHAPDF interface [87]. Both the LO and NLO PDF sets are obtained with  $\alpha_s(m_Z) = 0.118$ . The number of active flavours is set to  $N_F = 5$ . Unless stated otherwise, all results are presented using the NNPDF3.1 PDF set. Nevertheless, to assess the differences among various PDF sets we will also present our findings for the integrated fiducial NLO cross sections as obtained with the following PDF sets: CT10 [88], CT14 [89], CT18 [90], MSTW2008 [91], MMHT14 [92], MSHT20 [93], NNPDF3.0 [94], NNPDF4.0 [95] and ABMP16 [96]. For the central value of the renormalisation and factorisation scales we assume  $\mu_R = \mu_F = \mu_0$ . The scale uncertainties, however, are estimated by varying  $\mu_R$  and  $\mu_F$  independently in the following range

$$\left(\frac{\mu_R}{\mu_0}, \frac{\mu_F}{\mu_0}\right) = \{(2, 1), (0.5, 1), (1, 2), (1, 1), (1, 0.5), (2, 2), (0.5, 0.5)\}. \quad (3.7)$$

and choose the minimum and maximum of the resulting cross sections. The central values of the factorization and renormalisation scales have been set first to the following fixed scale setting

$$\mu_0 = m_t + \frac{1}{2}m_Z, \quad (3.8)$$

and subsequently the following dynamical scale choice is used

$$\mu_0 = \frac{1}{3}H_T, \quad (3.9)$$

where  $H_T$  is calculated on an event-by-event basis according to

$$H_T = p_{T,b_1} + p_{T,b_2} + p_{T,e^+} + p_{T,\mu^-} + p_{T,\tau^+} + p_{T,\tau^-} + p_T^{miss}. \quad (3.10)$$

The extra jet, even if resolved, is not included in the definition of the scale at NLO. Let us stress that the  $H_T$  based scale setting is blind to the fact that in the  $pp \rightarrow e^+ \nu_e \mu^- \bar{\nu}_\mu b \bar{b} \tau^+ \tau^-$  process Feynman diagrams with one or two top-quark resonances might appear. Nor does it assume anything about the  $Z$  boson. In other words, information about the underlying resonant structure of the event is not used at all.

## 4 Integrated fiducial cross sections

We begin our presentation of the results of our analysis with a discussion of the integrated fiducial cross section at the central value of the scale  $\mu_R = \mu_F = \mu_0 = m_t + m_Z/2$ . We first note that at the central scale the  $gg$  channel dominates the LO  $pp$  cross section by about 65% followed by the  $q\bar{q}$  channels with about 35%. With the input parameters and cuts specified in Section 3, we arrive at the following predictions

$$\begin{aligned} \sigma_{pp \rightarrow e^+ \nu_e \mu^- \bar{\nu}_\mu b \bar{b} \tau^+ \tau^-}^{\text{LO}}(\text{NNPDF3.1\_lo\_as\_0118}, \mu_0 = m_t + m_Z/2) &= 76.98_{-17.17}^{+24.30} (32\%) \text{ ab}, \\ \sigma_{pp \rightarrow e^+ \nu_e \mu^- \bar{\nu}_\mu b \bar{b} \tau^+ \tau^-}^{\text{NLO}}(\text{NNPDF3.1\_nlo\_as\_0118}, \mu_0 = m_t + m_Z/2) &= 97.86_{-6.16}^{+1.08} (1\%) \text{ ab}. \end{aligned} \quad (4.1)$$

The  $\mathcal{K}$ -factor, defined as the ratio of NLO to LO cross section, reads  $\mathcal{K} = 1.27$ . In our case both LO and NLO integrated fiducial cross sections are calculated for LO and NLO PDF sets as obtained

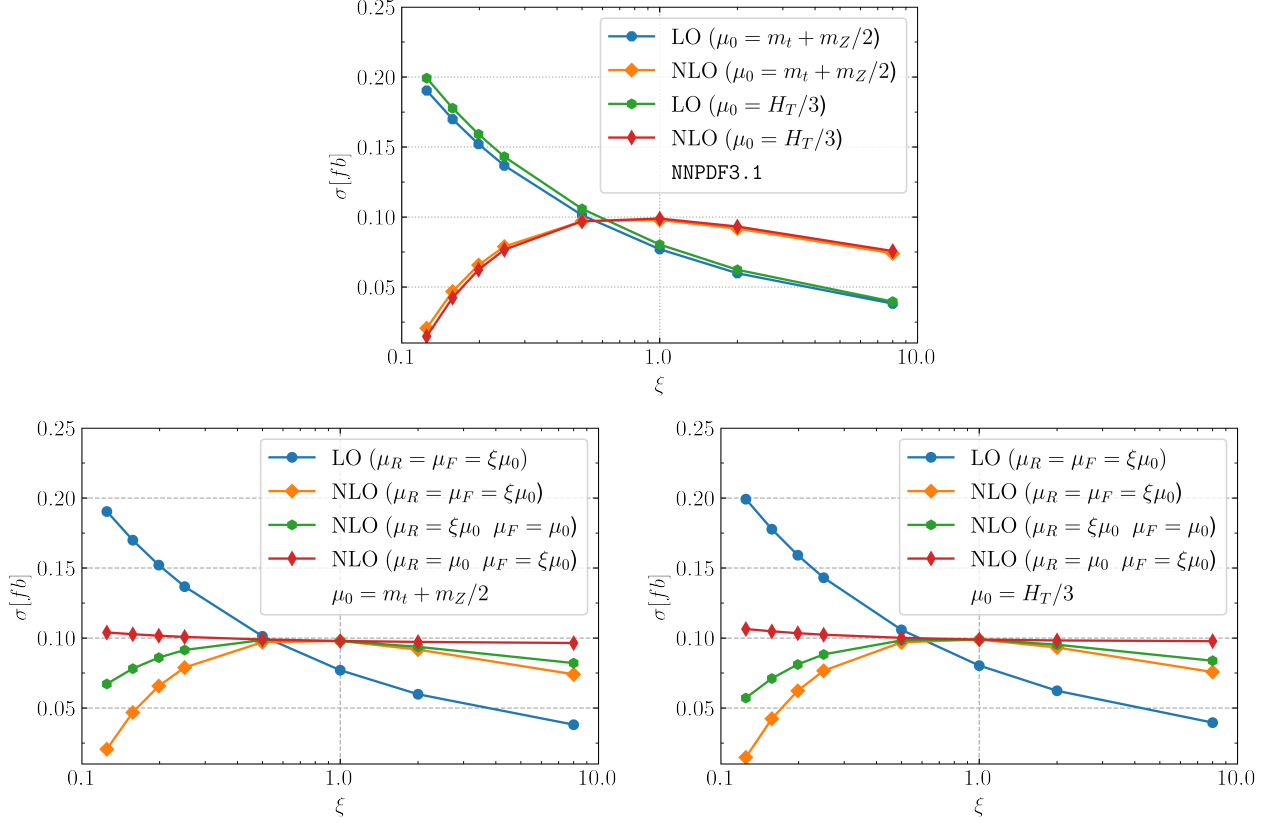


**Figure 3.** Scale dependence of the LO and NLO integrated fiducial cross sections for  $pp \rightarrow e^+ \nu_e \mu^- \bar{\nu}_\mu b \bar{b} \tau^+ \tau^- + X$  at the LHC with  $\sqrt{s} = 13$  TeV. In the upper plot renormalisation and factorisation scales are set to  $\mu_R = \mu_F = \xi \mu_0$  where  $\mu_0 = m_t + m_Z/2$  and  $\mu_0 = H_T/3$ . The LO and NLO NNPDF3.1 PDF sets are employed. In the two lower plots, the variation of  $\mu_R$  with fixed  $\mu_F$  and the reverse case are given for each case of  $\mu_0$ .

with  $\alpha_s(m_Z) = 0.118$ . Had we used the LO NNPDF3.1 PDF set with  $\alpha_s(m_Z) = 0.130$  or the NLO NNPDF3.1 PDF set also for our LO cross section we would rather have

$$\begin{aligned} \sigma_{pp \rightarrow e^+ \nu_e \mu^- \bar{\nu}_\mu b \bar{b} \tau^+ \tau^-}^{\text{LO}}(\text{NNPDF3.1\_lo\_as\_0130}, \mu_0 = m_t + m_Z/2) &= 86.96^{+30.13 (35\%)}_{-20.70 (24\%)} \text{ ab}, \\ \sigma_{pp \rightarrow e^+ \nu_e \mu^- \bar{\nu}_\mu b \bar{b} \tau^+ \tau^-}^{\text{LO}}(\text{NNPDF3.1\_nlo\_as\_0118}, \mu_0 = m_t + m_Z/2) &= 78.23^{+25.49 (33\%)}_{-17.85 (23\%)} \text{ ab}. \end{aligned} \quad (4.2)$$

These predictions result in a  $\mathcal{K}$ -factor of  $\mathcal{K} = 1.13$  and  $\mathcal{K} = 1.25$  respectively. Thus, NLO QCD corrections for the  $t\bar{t}Z$  process are below 30% for the fixed scale setting. The theoretical uncertainties resulting from scale variation taken as a maximum of the lower and upper bounds are of the order of 32% at LO and 6% at NLO. Moving from LO to NLO, the theoretical error is reduced by a factor larger than 5. Similar findings are obtained for the kinematical dependent scale setting. For  $\mu_R = \mu_F = \mu_0 = H_T/3$  we have

$$\begin{aligned} \sigma_{pp \rightarrow e^+ \nu_e \mu^- \bar{\nu}_\mu b \bar{b} \tau^+ \tau^-}^{\text{LO}}(\text{NNPDF3.1\_lo\_as\_0118}, \mu_0 = H_T/3) &= 80.32^{+25.51 (32\%)}_{-18.02 (22\%)} \text{ ab}, \\ \sigma_{pp \rightarrow e^+ \nu_e \mu^- \bar{\nu}_\mu b \bar{b} \tau^+ \tau^-}^{\text{NLO}}(\text{NNPDF3.1\_nlo\_as\_0118}, \mu_0 = H_T/3) &= 98.88^{+1.22 (1\%)}_{-5.68 (6\%)} \text{ ab}. \end{aligned} \quad (4.3)$$

In this case the  $\mathcal{K}$ -factor is slightly smaller, i.e. we have  $\mathcal{K} = 1.23$ . Had we used the LO NNPDF3.1 PDF set with  $\alpha_s(m_Z) = 0.130$  we would rather obtain  $\mathcal{K} = 1.09$  and finally with the NLO NNPDF3.1

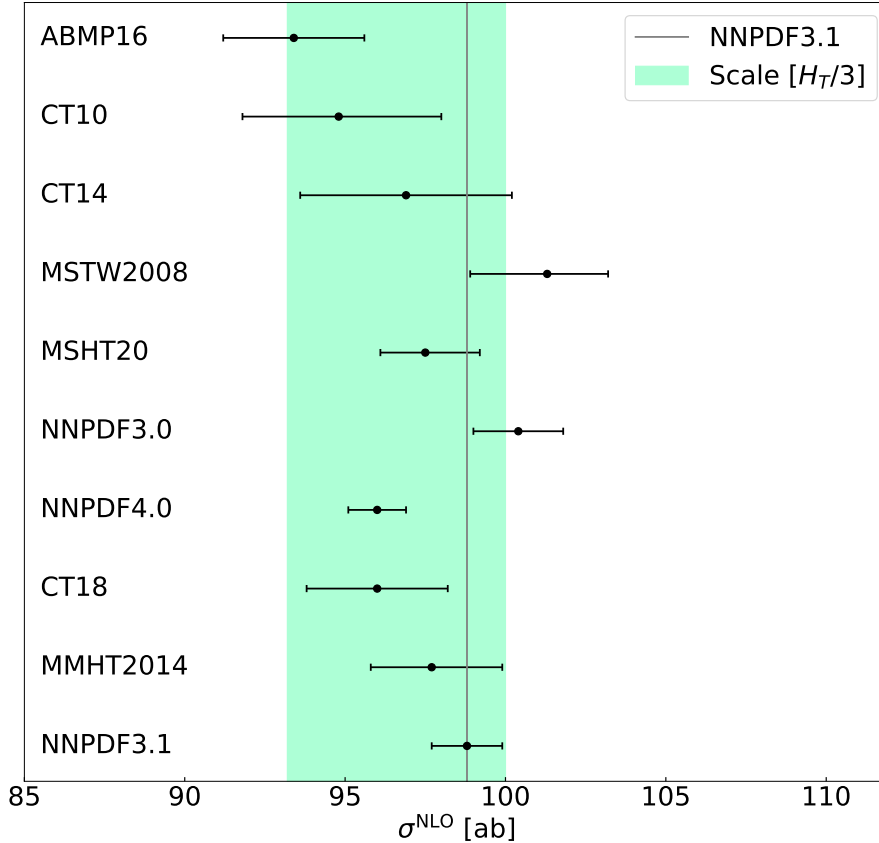


**Figure 4.** *NLO integrated fiducial cross sections for  $pp \rightarrow e^+ \nu_e \mu^- \bar{\nu}_\mu b \bar{b} \tau^+ \tau^- + X$  at the LHC with  $\sqrt{s} = 13$  TeV. Theoretical results are provided for  $\mu_R = \mu_F = \mu_0 = H_T/3$  as well as for various PDF sets. Scale uncertainties are reported for the NNPDF3.1 PDF set and are shown as a blue band.*

PDF we would have  $\mathcal{K} = 1.21$ . For the  $H_T$  based scale choice NLO QCD corrections are reduced, i.e. they are below 25%. The size of theoretical uncertainties remain the same.

Subsequently, we turn our attention to a graphical representation of the scale dependence for the integrated fiducial LO and NLO cross sections. In Figure 3 we present the behaviour of  $\sigma^{\text{LO}}$  and  $\sigma^{\text{NLO}}$  upon varying the central value of  $\mu_R$  and  $\mu_F$  by a factor of  $\xi \in \{0.125, \dots, 8\}$ . Both  $\mu_0 = m_t + m_Z/2$  and  $\mu_0 = H_T/3$  are shown, allowing us to compare the two scale settings. Also given in Figure 3 is the variation of  $\mu_R$  with the fixed value of  $\mu_F$  and the variation of  $\mu_F$  with fixed  $\mu_R$  for each case of  $\mu_0$  separately. We note that, as far as the integrated cross sections are concerned, both scale settings are similar and might be used in phenomenological applications. Furthermore, in the range employed for the scale variation, i.e. when  $\xi \in \{0.5, \dots, 2\}$ , the scale uncertainty is driven by the changes in  $\mu_R$ . Consequently, varying  $\mu_R$  and  $\mu_F$  simultaneously up and down by a factor of 2 around  $\mu_0$  would produce uncertainty bands very similar to those obtained using the full prescription of Eq. (3.7).

In the next step, while employing the dynamical scale  $\mu_R = \mu_F = \mu_0 = H_T/3$ , we examine the second main source of theoretical uncertainties at NLO in QCD, that comes from the choice of PDF. We use the corresponding prescription from each PDF fitting group to provide the 68% confidence level (C.L.) PDF uncertainties. For the default NNPDF3.1 PDF set they are at the 1% level. Comparable results have been obtained for NNPDF3.0 and NNPDF4.0. For the CT family (CT10, CT14 and CT18), on the other hand, we have received slightly higher PDF errors,  $\delta_{\text{PDF}} \in (2\% - 3\%)$ . For

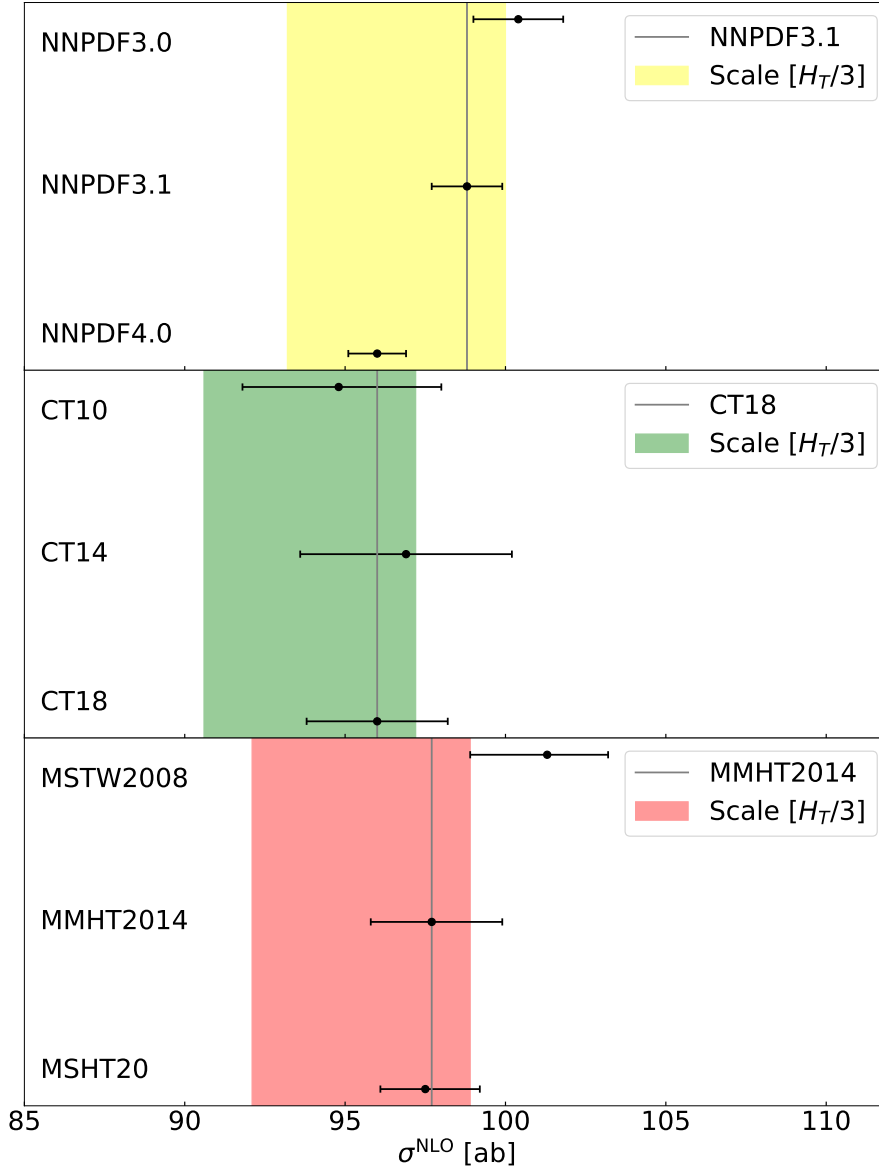


**Figure 5.** *NLO integrated fiducial cross sections for  $pp \rightarrow e^+ \nu_e \mu^- \bar{\nu}_\mu b \bar{b} \tau^+ \tau^- + X$  at the LHC with  $\sqrt{s} = 13$  TeV. Theoretical results are provided for  $\mu_R = \mu_F = \mu_0 = H_T/3$  as well as for various PDF sets. Scale uncertainties are reported for the NNPDF3.1 PDF set (yellow band), for CT18 (green band) as well as for MMHT2014 (red band).*

MSTW2008, MMHT2014 and MSHT20 as well as for ABMP16 the PDF uncertainties are consistently of the order of  $\delta_{\text{PDF}} = 2\%$ . Thus, the NNPDF PDF sets yield the smallest PDF uncertainties. Next, we compare the NLO integrated fiducial cross section obtained with the help of these PDFs to the result generated with the default setup. The largest difference with respect to our central predictions can be noticed for the ABMP16 PDF set. This result is smaller than the NNPDF3.1 prediction by 5%. For the CT18 (MMHT2014) PDF set we see differences at the level of 3% (1%), so comparable to the individual estimates of PDF systematics. By and large, the scale uncertainties are still the dominant source of theoretical error ( $\delta_{\text{scale}} = 6\%$  at NLO).

A graphical representation of these findings is given in Figure 4, where theoretical results are

SCALE	$p_{T,b}$	$\sigma^{\text{LO}}$ [ab]	$\delta_{\text{scale}}$	$\sigma^{\text{NLO}}$ [ab]	$\delta_{\text{scale}}$	$\delta_{\text{PDF}}$	$\mathcal{K} = \sigma^{\text{NLO}}/\sigma^{\text{LO}}$
$\mu_0 = m_t + m_Z/2$	25	76.98	+32% -22%	97.86	+1% -6%	+1% -1%	1.27
	30	71.36	+32% -22%	89.53	+1% -6%	+1% -1%	1.25
	35	65.19	+32% -22%	80.96	+1% -6%	+1% -1%	1.24
	40	58.84	+32% -22%	72.42	+1% -6%	+1% -1%	1.23
$\mu_0 = H_T/3$	25	80.32	+32% -22%	98.88	+1% -6%	+1% -1%	1.23
	30	74.22	+32% -22%	90.27	+1% -5%	+1% -1%	1.22
	35	67.52	+32% -22%	81.51	+1% -5%	+1% -1%	1.21
	40	60.61	+32% -22%	72.82	+1% -5%	+1% -1%	1.20

**Table 4.** LO and NLO integrated fiducial cross sections for the  $pp \rightarrow e^+ \nu_e \mu^- \bar{\nu}_\mu b \bar{b} \tau^+ \tau^- + X$  process at the LHC with  $\sqrt{s} = 13$  TeV. Results are evaluated using  $\mu_R = \mu_F = \mu_0$  where  $\mu_0 = H_T/3$  and  $\mu_0 = m_t + m_Z/2$ . The LO and NLO NNPDF3.1 PDF sets are used. We display results for four different values of the  $p_{T,b}$  cut. Also given are the theoretical uncertainties coming from scale variation ( $\delta_{\text{scale}}$ ) and PDFs ( $\delta_{\text{PDF}}$ ). In the last column the  $\mathcal{K}$ -factor is shown. Monte Carlo errors are at the permille or sub-permille level.

provided for  $\mu_R = \mu_F = \mu_0 = H_T/3$ . Scale uncertainties are reported for the NNPDF3.1 PDF set and are shown as a blue band. At the bottom of the plot we display the results for the three main global fitting groups: CT18, MMHT2014 and NNPDF3.1, which are commonly used to provide theoretical predictions for the LHC Run II. In this way we can see the relative difference between the various sets and the overall agreement. As a bonus of our study, in Figure 5 we show the NLO integrated fiducial cross sections for three main families of PDFs separately. We display NNPDF (NNPDF3.0, NNPDF 3.1 and NNPDF4.0), CTEQ-TEA (CT10, CT14 and CT18) as well as MSHT (MSTW2008, MMHT14 and MSHT20). In this way we can track the relative changes from the older versions to the newest ones within the given set. In the case of NNPDF sets, scale uncertainties are reported for the NNPDF3.1 PDF set (yellow band), for CTEQ-TEA PDFs they are provided for CT18 (green band) and finally for MSHT scale uncertainties are depicted for MMHT2014 (red band). For all three cases we obtain  $\delta_{\text{scale}} = \begin{smallmatrix} +1\% \\ -6\% \end{smallmatrix}$ . While the CT and MSHT PDF families show perfect agreement within the errors, the NNPDF4.0 result shows a small tension with the prediction obtained with the NNPDF3.1 PDF set. In other words, the evolution from NNPDF3.0 to NNPDF4.0 does not converge equally well as observed for the other PDF families. In all three cases, however, as expected the errors are reduced since the newer PDF sets include more data in their respective fits. On the other hand, when comparing the most recent PDF sets, i.e. NNPDF4.0, CT18 and MSHT20, we observe that the obtained results are in perfect agreement within the corresponding errors.

A stability test of LO and NLO fiducial cross sections with respect to the  $b$ -jet transverse momentum cut is shown in Table 4. The cut is varied in steps of 5 GeV within the following range:  $p_{T,b} \in (25 - 40)$  GeV. We also show theoretical uncertainties as estimated from the scale variation and from PDFs as well as the  $\mathcal{K}$ -factor. We notice that NLO QCD corrections are almost constant in size for the  $p_{T,b}$  cut within the tested range. In addition, NLO QCD predictions show a very stable

$ M_{\tau^+\tau^-} - m_Z  < X$	$\sigma^{\text{LO}}$ [ab]	$\delta_{\text{scale}}$	$\sigma^{\text{NLO}}$ [ab]	$\delta_{\text{scale}}$	$\delta_{\text{PDF}}$	$\mathcal{K} = \sigma^{\text{NLO}}/\sigma^{\text{LO}}$
$\mu_0 = m_t + m_Z/2$						
–	76.98	+32% –22%	97.86	+1% –6%	+1% –1%	1.27
25 GeV	71.06	+32% –22%	90.10	+1% –6%	+1% –1%	1.27
20 GeV	70.26	+32% –22%	89.07	+1% –6%	+1% –1%	1.27
15 GeV	69.10	+32% –22%	87.57	+1% –6%	+1% –1%	1.27
10 GeV	66.99	+32% –22%	84.90	+1% –6%	+1% –1%	1.27
$\mu_0 = H_T/3$						
–	80.32	+32% –22%	98.88	+1% –6%	+1% –1%	1.23
25 GeV	74.06	+32% –22%	91.00	+1% –6%	+1% –1%	1.23
20 GeV	73.22	+32% –22%	89.96	+1% –6%	+1% –1%	1.23
15 GeV	72.00	+32% –22%	88.44	+1% –6%	+1% –1%	1.23
10 GeV	69.81	+32% –22%	85.74	+1% –6%	+1% –1%	1.23

**Table 5.** LO and NLO integrated fiducial cross sections for the  $pp \rightarrow e^+\nu_e \mu^-\bar{\nu}_\mu \tau^+\tau^- b\bar{b} + X$  process at the LHC with  $\sqrt{s} = 13$  TeV. Results are evaluated using  $\mu_R = \mu_F = \mu_0$  with  $\mu_0 = m_t + m_Z/2$  and  $\mu_0 = H_T/3$ . The LO and NLO NNPDF3.1 PDF sets are used. We display results for four different values of the  $M_{\tau^+\tau^-}$  cut, where  $|M_{\tau^+\tau^-} - m_Z| < X$  with  $X \in (25, 20, 15, 10)$  GeV. Additionally, the LO and NLO predictions without this requirement are given. The theoretical uncertainties coming from scale variation ( $\delta_{\text{scale}}$ ) and PDFs ( $\delta_{\text{PDF}}$ ) are also provided. In the last column the K-factor is shown. Monte Carlo errors are at the permille or sub-permille level.

behaviour with respect to both sources of theoretical uncertainties.

In Table 5, on the other hand, we give LO and NLO integrated fiducial cross sections for four different values of the cut on the invariant mass of the  $\tau^+\tau^-$  pair. We require  $M_{\tau^+\tau^-}$  to be in the following  $Z$  boson mass window,  $|M_{\tau^+\tau^-} - m_Z| < X$ , where  $X \in \{25, 20, 15, 10\}$  GeV. The latter set covers the values frequently used in different experimental analyses for the process. This requirement favours configurations where the  $\tau$  lepton pair originates from a decaying  $Z$  boson with possible interferences induced by a very off-shell photon in the same mass window. We compare these theoretical predictions to the result without this condition. We notice that already for the smallest window, i.e. for  $|M_{\tau^+\tau^-} - m_Z| < 10$  GeV, we can recover 87% of the full  $pp$  cross section for the  $pp \rightarrow e^+\nu_e \mu^-\bar{\nu}_\mu \tau^+\tau^- b\bar{b} + X$  process. For the enlarged window of 25 GeV this number is instead 92%. Moreover, the NLO QCD corrections are extremely stable with respect to this cut, regardless of the window size applied around the nominal  $Z$  boson mass. We shall use this cut at a later time, when we compare our state-of-the-art theoretical predictions with those calculated in the NWA.

Finally, we also provide theoretical predictions for a slightly modified setup. Specifically, the following more exclusive set of selection cuts is additionally imposed on the final state charged leptons

SCALE	ORDER	PDF	$\sigma$ [ab]	$\mathcal{K} = \sigma^{\text{NLO}}/\sigma^{\text{LO}}$
$\mu_0 = m_t + m_Z/2$	LO	NNPDF3.1_lo_as_0130	$29.74^{+35\%}_{-24\%}$	1.06
	LO	NNPDF3.1_lo_as_0118	$26.34^{+32\%}_{-23\%}$	1.19
	LO	NNPDF3.1_nlo_as_0118	$26.84^{+33\%}_{-23\%}$	1.17
	NLO	NNPDF3.1_nlo_as_0118	$31.44^{+1\%}_{-5\%}$	—
$\mu_0 = H_T/3$	LO	NNPDF3.1_lo_as_0130	$30.15^{+35\%}_{-24\%}$	1.05
	LO	NNPDF3.1_lo_as_0118	$26.66^{+32\%}_{-23\%}$	1.18
	LO	NNPDF3.1_nlo_as_0118	$27.14^{+33\%}_{-23\%}$	1.16
	NLO	NNPDF3.1_nlo_as_0118	$31.55^{+1\%}_{-5\%}$	—

**Table 6.** LO and NLO integrated fiducial cross sections for the  $pp \rightarrow e^+ \nu_e \mu^- \bar{\nu}_\mu b \bar{b} \tau^+ \tau^- + X$  process at the LHC with  $\sqrt{s} = 13$  TeV. Results are evaluated for the more exclusive setup, which considers the cuts of Eq. (4.4) on top of the standard kinematical cuts, using  $\mu_R = \mu_F = \mu_0$  where  $\mu_0 = m_t + m_Z/2$  and  $\mu_0 = H_T/3$ . Three PDF sets are employed for LO predictions with different values of  $\alpha_s(m_Z)$ . In the last column the  $\mathcal{K}$ -factor, defined as  $\sigma^{\text{NLO}}/\sigma^{\text{LO}}$ , is shown. Monte Carlo errors are at the permille or sub-permille level.

and  $b$ -jets:

$$p_{T,b} > 40 \text{ GeV}, \quad p_{T,\ell} > 30 \text{ GeV}, \quad \Delta R_{b\ell} > 0.4. \quad (4.4)$$

These more exclusive selection cuts are motivated by the various experimental analysis carried out by ATLAS and CMS collaborations for the  $pp \rightarrow t\bar{t}Z$  process, see e.g. Refs. [1–4]. The LO and NLO integrated fiducial cross sections for both scale settings calculated with these modified cuts are presented in Table 6. When comparing to the default setup we notice the reduced size of NLO QCD corrections. Specifically, they are now below 20%. With the NNPDF3.1-lo-as-0130 LO PDF set, however, they are as small as 5% – 6%. On the other hand, theoretical uncertainties due to the scale variation remain the same. Similarly to the default setup also here such differences in the  $\mathcal{K}$ -factor are driven by changes in the LO cross section and in particular, by changes in the value of  $\alpha_s(m_Z)$  used as an input parameter in the corresponding LO NNPDF3.1 PDF set. We also note, that employing LO and NLO NNPDF3.1 PDF sets with the same value of  $\alpha_s(m_Z)$  for the LO cross section results in very similar predictions for the process at hand.

To summarise this part, for the integrated fiducial cross sections, where effects of the phase-space regions close to the particle threshold for  $t\bar{t}Z$  production dominate, both scale choices that we employed describe the  $pp \rightarrow e^+ \nu_e \mu^- \bar{\nu}_\mu b \bar{b} \tau^+ \tau^- + X$  process very well. They agree within their respective theoretical errors and have similar theoretical systematics. Thus, a choice between a fixed and dynamical scale setting does not play a crucial role. On the other hand, for the differential cross sections the off-shell effects of the top quarks and massive gauge bosons as well as the single- and non-resonant contributions become more important, making the usage of the dynamical scale setting a necessity. We will come back to this point in Section 5.

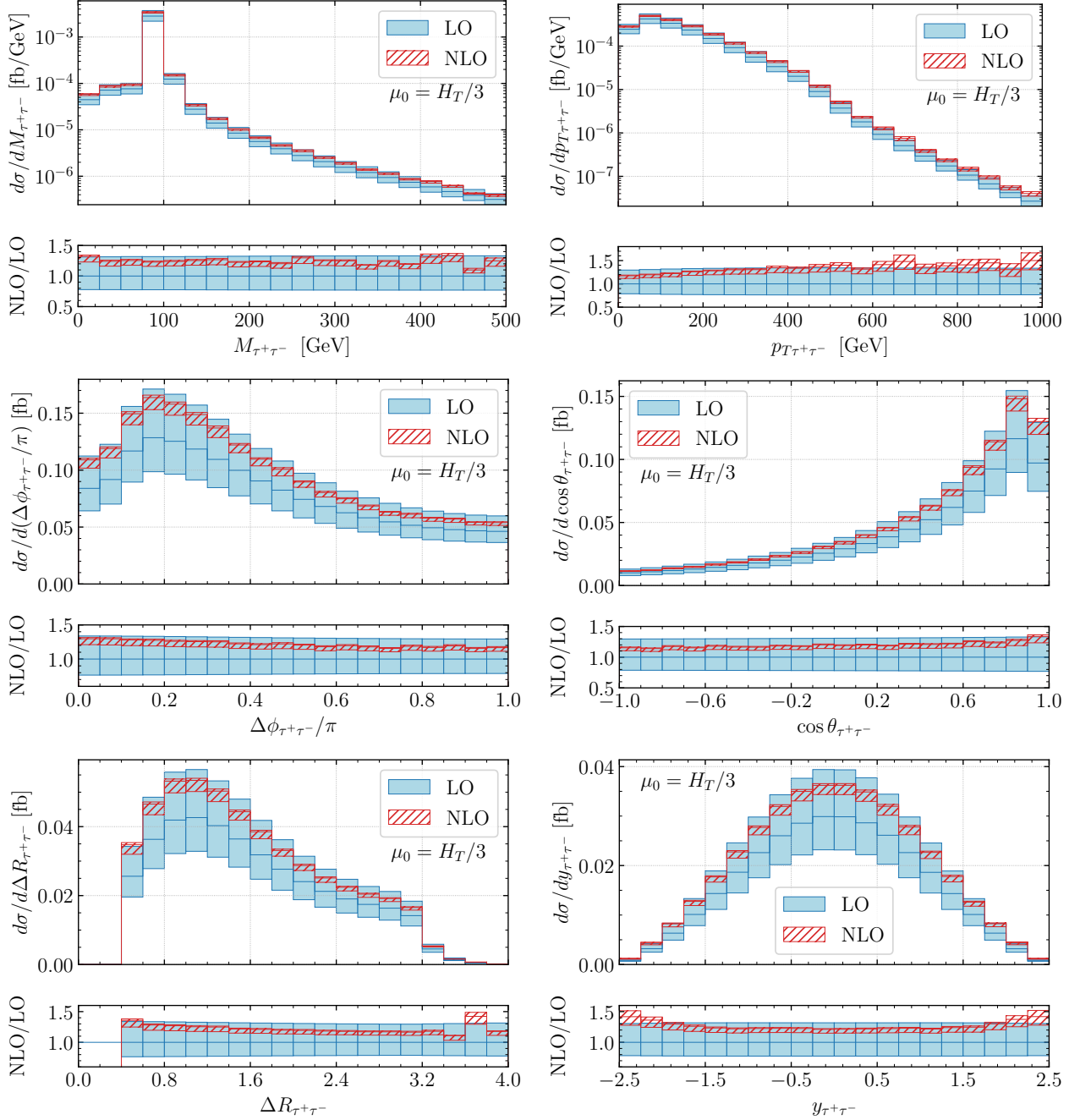


**Figure 6.** Differential cross-section distributions for  $pp \rightarrow e^+ \nu_e \mu^- \bar{\nu}_\mu b \bar{b} \tau^+ \tau^- + X$  at the LHC with  $\sqrt{s} = 13$  TeV as a function of  $M_{\tau^+\tau^-}$ ,  $p_{T\tau^+\tau^-}$ ,  $\Delta\phi_{\tau^+\tau^-}$ ,  $\cos\theta_{\tau^+\tau^-}$ ,  $\Delta R_{\tau^+\tau^-}$  and  $y_{\tau^+\tau^-}$ . The blue curve corresponds to the LO and the red curve to the NLO result. Also shown are the corresponding uncertainty bands resulting from scale variations. The lower panels display the differential K-factor together with the uncertainty band and the relative scale uncertainties of the LO cross section. The scale choice is  $\mu_R = \mu_F = \mu_0 = H_T/3$ . The cross sections are evaluated with the NNPDF3.1 PDF sets.

## 5 Differential fiducial cross sections

Integrated cross sections are mostly influenced by final-state production relatively close to the threshold as defined by particle masses. On the other hand, differential cross sections extend themselves up to

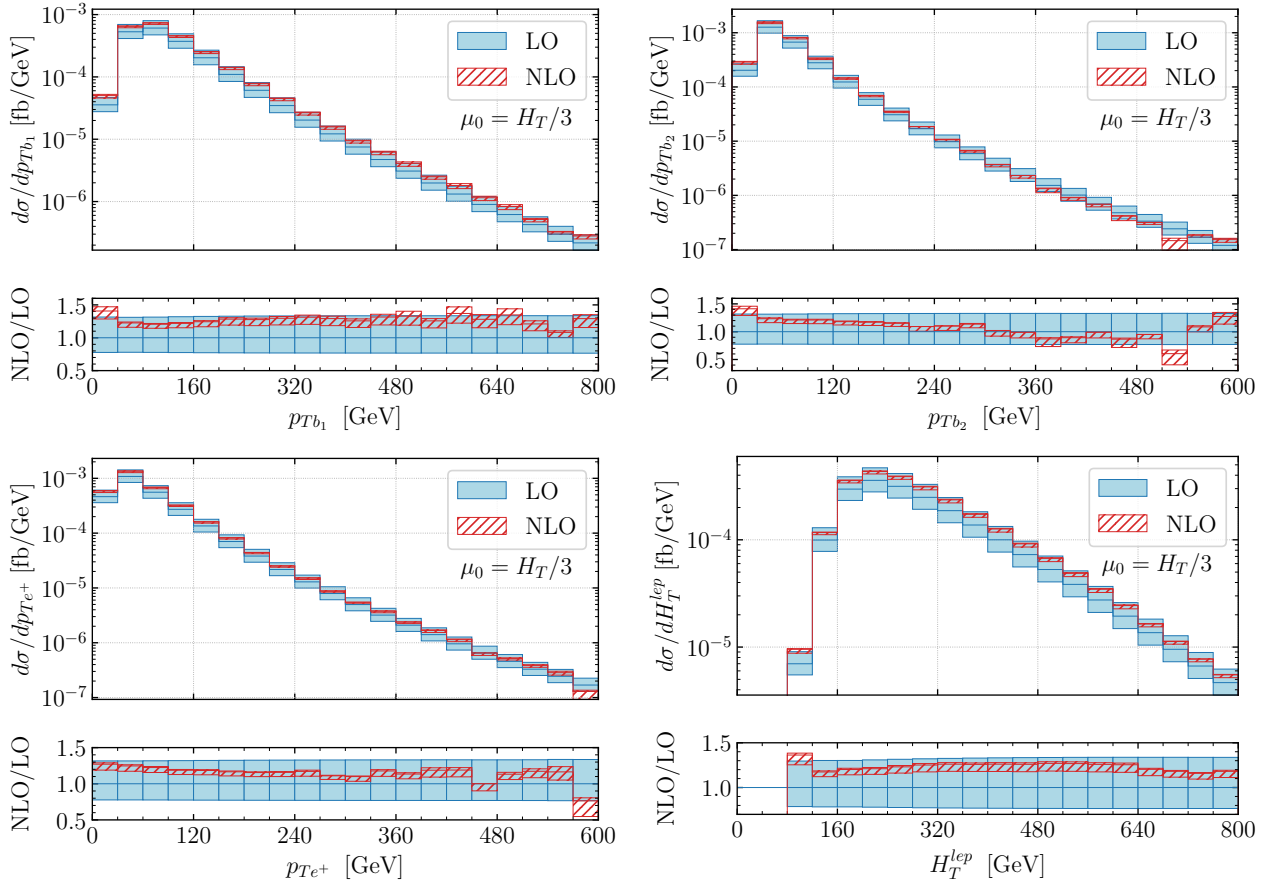


**Figure 7.** Differential cross-section distributions for  $pp \rightarrow e^+ \nu_e \mu^- \bar{\nu}_\mu b \bar{b} \tau^+ \tau^- + X$  at the LHC with  $\sqrt{s} = 13$  TeV as a function of  $p_{Tb_1}$ ,  $p_{Tb_2}$ ,  $p_{Te^+}$  and  $H_T^{lep}$ . The blue curve corresponds to the LO and the red curve to the NLO result. Also shown are the corresponding uncertainty bands resulting from scale variations. The lower panels display the differential  $\mathcal{K}$ -factor together with the uncertainty band and the relative scale uncertainties of the LO cross section. The scale choice is  $\mu_R = \mu_F = \mu_0 = H_T/3$ . The cross sections are evaluated with the NNPDF3.1 PDF sets.

energy scales that are much larger than the threshold, and may show larger shape distortions in such high-energy regions. Therefore, in the next step we turn our attention to the differential cross section distributions for the  $pp \rightarrow e^+ \nu_e \mu^- \bar{\nu}_\mu b \bar{b} \tau^+ \tau^- + X$  process. In the following, we examine the size of the NLO QCD corrections to the relevant observables at the LHC using our default setup with LO and NLO NNPDF3.1 PDF sets obtained with  $\alpha_s(m_Z) = 0.118$ . Had we used the same NLO NNPDF3.1 PDF set also for the LO predictions our results and conclusions that we provide below would not change significantly. For each plot the upper panels always show absolute LO and NLO predictions together with the corresponding scale uncertainty bands. The lower panels display the differential  $\mathcal{K}$ -factor together with its scale uncertainty band as well as the relative scale uncertainties of the LO cross section. Specifically, we plot

$$\mathcal{K}^{\text{NLO}}(\mu) = \frac{d\sigma^{\text{NLO}}(\mu)/dX}{d\sigma^{\text{LO}}(\mu_0)/dX}, \quad \text{and} \quad \mathcal{K}^{\text{LO}}(\mu) = \frac{d\sigma^{\text{LO}}(\mu)/dX}{d\sigma^{\text{LO}}(\mu_0)/dX}, \quad (5.1)$$

where  $\mu_0$  is the central value of the scale and  $X$  denotes the observable under consideration. The error band is determined similarly to the integrated cross section case, i.e. with the help of a 7-point

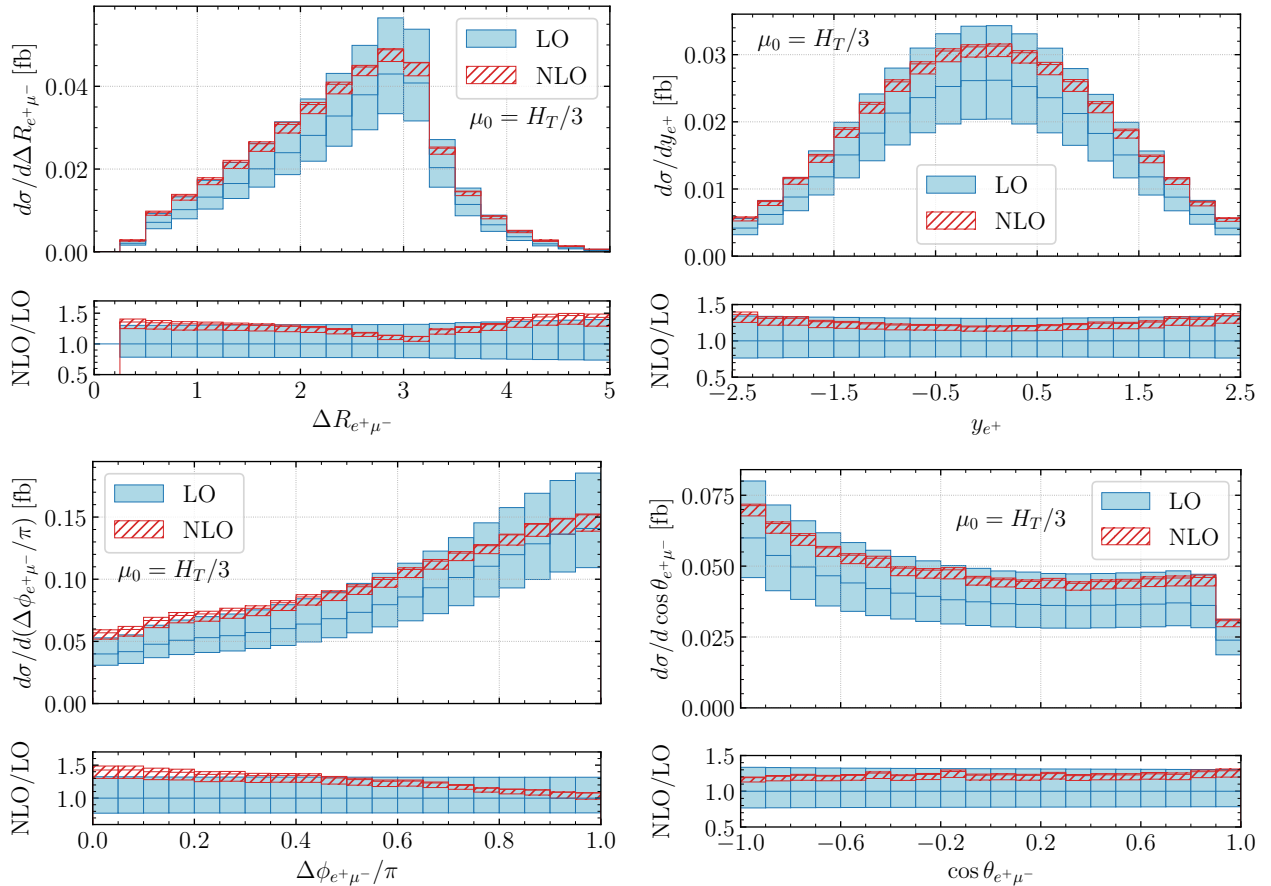


**Figure 8.** Differential cross-section distributions for  $pp \rightarrow e^+ \nu_e \mu^- \bar{\nu}_\mu b \bar{b} \tau^+ \tau^- + X$  at the LHC with  $\sqrt{s} = 13$  TeV as a function of  $\Delta R_{e^+ \mu^-}$ ,  $y_{e^+}$ ,  $\cos \theta_{e^+ \mu^-}$  and  $\Delta \phi_{e^+ \mu^-}$ . The blue curve corresponds to the LO and the red curve to the NLO result. Also shown are the corresponding uncertainty bands resulting from scale variations. The lower panels display the differential  $\mathcal{K}$ -factor together with the uncertainty band and the relative scale uncertainties of the LO cross section. The scale choice is  $\mu_R = \mu_F = \mu_0 = H_T/3$ . The cross sections are evaluated with the NNPDF3.1 PDF sets.

scale variation. We provide our results at the differential level only for the dynamical scale setting, i.e. for  $\mu_R = \mu_F = \mu_0 = H_T/3$ . The reason for that is as follows. For the fixed scale choice that we employed, i.e. for  $\mu_0 = m_t + m_Z/2$ , we could observe that for some choices of the  $\xi$  parameter, where  $\mu_R = \mu_F = \xi \mu_0$ , the NLO results become negative. This happens in the high-energy tails of dimensionful distributions. Furthermore, there are kinematic regions where the scale variation bands at LO and NLO do not overlap anymore. In addition, it can even happen that the scale variation at NLO actually exceeds the scale variation of the LO predictions. All these effects have already been observed in our previous studies for the  $t\bar{t} + X$  process, where  $X = j, \gamma, Z(\nu\bar{\nu}), W^\pm, H$  [49, 97–100]. They might be accommodated by a judicious choice of a dynamical scale setting<sup>1</sup>.

We start with the observables constructed from the two  $\tau$  leptons originating from the  $Z/\gamma^*$  boson decay. In Figure 6 we show differential cross sections as a function of the invariant mass of the  $\tau^+ \tau^-$  system,  $M_{\tau^+ \tau^-}$ , the transverse momentum of the  $\tau^+ \tau^-$  system,  $p_{T, \tau^+ \tau^-}$  and the azimuthal separation

<sup>1</sup>We note, however, that for the missing transverse momentum,  $p_T^{miss}$  (not shown here), the fixed scale setting performs better. Similar results have already been observed in the case of the  $pp \rightarrow e^+ \nu_e \mu^- \bar{\nu}_\mu b \bar{b} \nu_\tau \bar{\nu}_\tau + X$  process and discussed in Ref. [49].

between the two  $\tau$  leptons in the plane transverse to the beam,  $\Delta\phi_{\tau^+\tau^-}$ . The latter is always taken in such a way as to ensure  $0 \leq \Delta\phi_{\tau^+\tau^-} \leq \pi$ , consequently, we display  $\Delta\phi_{\tau^+\tau^-}/\pi$ . Furthermore, we present the cosine of the angle between the two  $\tau$  leptons,  $\cos\theta_{\tau^+\tau^-}$ , where the angle  $\theta_{\tau^+\tau^-}$  is given by  $\hat{p}_{\tau^+} \cdot \hat{p}_{\tau^-} = \cos\theta_{\tau^+\tau^-}$ . Also given are the rapidity-azimuthal-angle distance between the two  $\tau$  leptons,  $\Delta R_{\tau^+\tau^-}$  and the rapidity of the  $\tau^+\tau^-$  system,  $y_{\tau^+\tau^-}$ . For  $M_{\tau^+\tau^-}$ , in the vicinity of the  $Z$  resonance as well as outside of the  $Z$  boson peak, the NLO QCD corrections are similar in size and significant. Specifically, they are of the order of 10% – 30%. The inclusion of higher-order corrections reduces the scale dependence from 33% to 8% for our dynamical scale setting. For the transverse momentum of the  $\tau^+\tau^-$  pair the NLO corrections vary between 17% and 50% introducing shape distortions at the level of 33%. Also the NLO theoretical uncertainties are slightly larger for this observable up to 13%. In the case of the following two dimensionless observables,  $\Delta\phi_{\tau^+\tau^-}/\pi$  and  $\cos\theta_{\tau^+\tau^-}$  we observe a similar reduction of the theoretical scale uncertainty from around 30% at LO to 8% at NLO after the inclusion of NLO QCD effects. The NLO QCD corrections can go up to about 35%, introducing the overall shape distortions not larger than 20%. The situation is slightly different for  $\Delta R_{\tau^+\tau^-}$ , for which we received larger NLO QCD corrections up to about 40% and shape distortions of the order of 30%. At last, for  $y_{\tau^+\tau^-}$  in the central rapidity regions higher order effects are of the order of 20%. At forward and backward rapidity regions, on the other hand, they increased to 30% – 40%. For the last two observables NLO scale uncertainties are below 10%.

Similar to the integrated fiducial cross sections we observe a strong reduction in the unphysical scale dependence when NLO QCD corrections are included. Moreover, scale dependence bands for LO and NLO predictions indicate a well behaved perturbative convergence. However, even with our dynamical scale setting the NLO QCD corrections to the differential cross-section distributions, are significant. In a few cases shape distortions are comparable in size to the LO theoretical uncertainties, i.e. they are of the order of 30%. Thus, a suitably chosen global  $\mathcal{K}$ -factor can not be applied to all LO predictions at the same time to obtain results that approximate well the full NLO QCD predictions. As such, full NLO predictions should be used consistently. Furthermore, because of the key role of the top quark interaction with the  $Z$  boson in many beyond the Standard Model (BSM) scenarios, theoretical predictions for benchmark observables calculated within the SM framework must be provided as accurately as possible. A realistic assessment of systematic uncertainties for these theoretical predictions is required as well. Various differential fiducial cross-section distributions might be modified by anomalous  $t\bar{t}Z$  couplings. Thus, it is vital to have the SM predictions under excellent theoretical control. We note that, from the observables that have been presented,  $p_{T\tau^+\tau^-}$  and  $\Delta\phi_{\tau^+\tau^-}$  are particularly interesting as they have already proved to be good analysers of the  $t\bar{t}Z$  coupling, see e.g. Refs. [12, 15, 16].

In the next step we look at observables related to the two top quarks. They are especially important from the point of view of the modelling of top-quark decays. In Figure 7 we present the following dimensionful observables: the transverse momentum of the hardest  $b$ -jet,  $p_{Tb_1}$ , the transverse momentum of the second hardest  $b$ -jet,  $p_{Tb_2}$ , the transverse momentum of the positron,  $p_{Te^+}$  and the scalar sum of the transverse momenta of the charged leptons,  $H_T^{lep}$ . The last observable is defined as follows

$$H_T^{lep} = p_{Te^+} + p_{T\mu^-} + p_{T\tau^+} + p_{T\tau^-}. \quad (5.2)$$

NLO QCD corrections for the  $b$ -jet related observables,  $p_{Tb_1}$  and  $p_{Tb_2}$ , go up to 40%, whereas for the leptonic observables these corrections are below 30%, excluding the second bin in  $H_T^{lep}$  which goes up to about 40%. NLO theoretical uncertainties for all these observables are similar and around 10%, even though they can be larger for a few single bins and reach up to 30%.

Finally, in Figure 8 angular correlations of the leptons coming from the top-quark decays are displayed. Specifically, we show the rapidity-azimuthal-angle distance between the positron and muon,  $\Delta R_{e+\mu-}$ , the rapidity of the positron,  $y_{e+}$ , the azimuthal angle between the positron and muon in the transverse plane,  $\Delta\phi_{e+\mu-}$ , and the cosine of the angle between them,  $\cos\theta_{e+\mu-}$ . These observables are also sensitive to various BSM models, however, they are mostly used to study spin correlations in top-quark decays. We can observe that compared to similar observables for the  $\tau^+\tau^-$  system, the shapes are vastly different here. This of course is not surprising given that the positron and muon are predominantly produced in back-to-back configurations. NLO QCD corrections for dimensionless observables constructed from the two charged leptons originating from the top quarks are not small. Specifically, for  $\Delta R_{e+\mu-}$  they are up to 45%, for  $y_{e+}$  in the central rapidity regions they are of the order of 20% whereas in the forward and backward regions they increase up to about 40%. In the case of  $\Delta\phi_{e+\mu-}$  higher-order effects are below 40% and finally for  $\cos\theta_{e+\mu-}$  NLO QCD corrections are of the order of 25%. For all four differential cross-section distributions theoretical uncertainties coming from scale variation are reduced from 30% – 40% at LO to maximally up to 10% at NLO in QCD.

Having examined the size of scale uncertainties for the differential cross section distributions we turn our attention to the PDF uncertainties. We have already checked that the latter are smaller than the theoretical uncertainties stemming from scale variation at the integrated fiducial level. We would like to check whether this is still the case at the differential level. We display the six observables that have been shown previously. Specifically, in Figure 9 we present differential cross section distributions as a function of  $\Delta\phi_{\tau^+\tau^-}$ ,  $y_{\tau^+\tau^-}$ ,  $\cos\theta_{\tau^+\tau^-}$ ,  $\Delta R_{\tau^+\tau^-}$ ,  $M_{\tau^+\tau^-}$  and  $p_{T\tau^+\tau^-}$ . We plot them afresh for the CT18 and MMHT14 PDF sets. Each plot comprises three panels. The upper panel displays the absolute NLO prediction for three different PDF sets at the central scale value,  $\mu_R = \mu_F = \mu_0 = H_T/3$ . The middle panel shows the NLO QCD scale dependence band normalised to the NLO prediction for  $\mu_0$  and NNPDF3.1. Also given is the ratio of NLO QCD predictions generated for CT18 and MMHT14 to the default NNPDF3.1 PDF set. The lower panel exhibits the internal PDF uncertainties for each PDF set separately, which are also normalised to central NLO predictions with NNPDF3.1

We observe that also at the differential level the NNPDF3.1 PDF uncertainties are very small and well below the corresponding theoretical uncertainties due to scale dependence. Indeed, the internal NNPDF3.1 PDF uncertainties are maximally up to 1.5% for dimensionless observables and for  $M_{\tau^+\tau^-}$ . At the same time scale uncertainties are up to 7% – 10% for these observables. For  $p_{T\tau^+\tau^-}$ , the last observable that we have shown, the NNPDF3.1 PDF uncertainties in the tails of the distribution do not exceed 5% – 6%. However, these are phase-space regions where the scale uncertainties can be as large as 13%. When analysing the internal PDF uncertainties for CT18 and MMHT14 we notice that they behave similarly and their PDF uncertainties are almost a factor of 2 larger than those for NNPDF3.1. This is true for MMHT14 for all observables except for  $p_{T\tau^+\tau^-}$  where the PDF uncertainties are not bigger than 6% and thus comparable to those from NNPDF3.1. In all cases, the selected PDF sets are still within the theoretical uncertainties due to scale dependence for all observables. Looking at the theoretical predictions for MMHT14 and CT18, we note that the relative difference to the NNPDF3.1 result is of the order of 1.5% and 4% respectively. Therefore, the PDF uncertainties are of a similar size as the difference between the results obtained using various PDF sets.

## 6 Off-shell vs on-shell modelling of top quarks and gauge bosons

In order to examine the size of the non-factorisable corrections for the  $pp \rightarrow e^+\nu_e\mu^-\bar{\nu}_\mu b\bar{b}\tau^+\tau^- + X$  process within our setup we compare the NLO QCD results with full off-shell effects included with the calculations in the NWA. The latter results are also generated with the help of the HELAC-

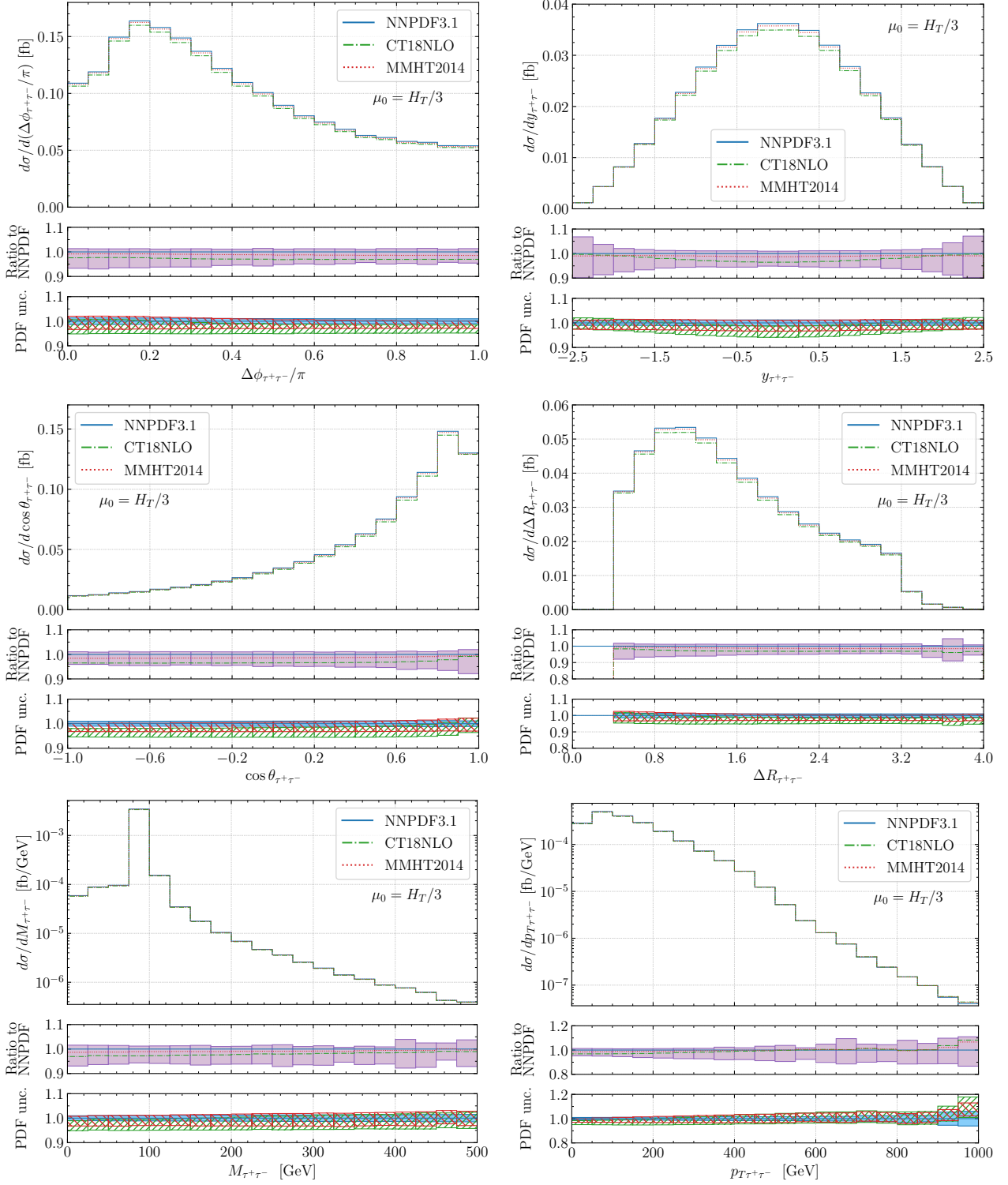


**Figure 9.** Differential cross-section distributions for  $pp \rightarrow e^+ \nu_e \mu^- \bar{\nu}_\mu b \bar{b} \tau^+ \tau^- + X$  at the LHC with  $\sqrt{s} = 13$  TeV as a function of  $\Delta\phi_{\tau^+\tau^-}$ ,  $y_{\tau^+\tau^-}$ ,  $\cos\theta_{\tau^+\tau^-}$ ,  $\Delta R_{\tau^+\tau^-}$ ,  $M_{\tau^+\tau^-}$  and  $p_{T,\tau^+\tau^-}$ . The upper panel shows the absolute NLO QCD predictions for three different PDF sets with  $\mu_R = \mu_F = \mu_0 = H_T/3$ . The middle panel displays the ratio to the result with the default NNPDF3.1 PDF set as well as its scale dependence. The lower panel presents the internal PDF uncertainties calculated separately for each PDF set.

NLO program [101], which recently has been extended to provide theoretical predictions also in this approximation. The NWA results at NLO in QCD are divided in two categories: the full NWA and the NWA with LO top-quark decays (hereafter referred to as  $\text{NWA}_{\text{full}}$  and  $\text{NWA}_{\text{LOdec}}$  respectively). The full NWA comprises NLO QCD corrections to both  $t\bar{t}Z$  production and the subsequent top-quark decays preserving at the same time the  $t\bar{t}$  spin correlations at the same accuracy. The  $\text{NWA}_{\text{LOdec}}$  case contains the results with NLO QCD corrections to the production stage only, whereas top-quark decays are calculated at LO. In this case  $t\bar{t}$  spin correlations are only available with LO accuracy. For consistency these findings are calculated with  $\Gamma_{t,\text{NWA}}^{\text{LO}}$ . The contribution from the  $t \rightarrow WbZ$  decay are neglected due to the tiny available phase space and the size of the  $t \rightarrow WbZ$  branching ratio. With the input parameters and cuts specified in Section 3, our findings can be summarised as follows

$$\sigma_{\text{NWA}}^{\text{LO}}(\text{NNPDF3.1\_lo\_as\_0118}, \mu_0 = H_T/3) = 72.69_{-16.24(22\%)}^{+22.97(32\%)} \text{ ab}, \quad (6.1)$$

$$\sigma_{\text{NWA}_{\text{full}}}^{\text{NLO}}(\text{NNPDF3.1\_nlo\_as\_0118}, \mu_0 = H_T/3) = 88.75_{-4.87(5\%)}^{-2.16(2\%)} \text{ ab}. \quad (6.2)$$

In the case where NLO QCD corrections to top-quark decays are omitted we obtain instead

$$\sigma_{\text{NWA}_{\text{LOdec}}}^{\text{NLO}}(\text{NNPDF3.1\_nlo\_as\_0118}, \mu_0 = H_T/3) = 96.74_{-9.98(10\%)}^{+7.21(7\%)} \text{ ab}. \quad (6.3)$$

We can immediately make the following conclusions based on our NWA results. First, we can see that the  $\text{NWA}_{\text{full}}$  prediction has the same theoretical uncertainties due to the scale dependence as the full off-shell result (see Eq. (4.3)). At LO they are at the level of 32% (to be compared to 32% for the full-off shell case), while at NLO in QCD they are reduced to 5% (6% for the full off-shell prediction). The size of NLO QCD corrections is also similar. Indeed, we find  $\mathcal{K} = \sigma_{\text{NWA}_{\text{full}}}^{\text{NLO}}/\sigma_{\text{NWA}}^{\text{LO}} = 1.22$  for our dynamical scale setting ( $\mathcal{K} = \sigma_{\text{off-shell}}^{\text{NLO}}/\sigma_{\text{off-shell}}^{\text{LO}} = 1.23$ ). When the higher-order corrections in top-quark decays are omitted, however, the scale dependence increases and theoretical uncertainties are at the level of 10%. Therefore, they are almost a factor of 2 larger than the theoretical uncertainty estimate for the  $\text{NWA}_{\text{full}}$  case. In addition, the NLO QCD corrections are larger as well for this case as we have  $\mathcal{K} = \sigma_{\text{NWA}_{\text{LOdec}}}^{\text{NLO}}/\sigma_{\text{NWA}}^{\text{LO}} = 1.33$ . Having both results  $\sigma_{\text{NWA}_{\text{full}}}^{\text{NLO}}$  and  $\sigma_{\text{NWA}_{\text{LOdec}}}^{\text{NLO}}$  we can furthermore assess that higher-order QCD corrections to top-quark decays are negative and of the order of 9%. We observe that  $\text{NWA}_{\text{LOdec}}$  is very close to the full off-shell prediction, and the two results agree well within the estimated uncertainties. We stress that this agreement is accidental and is an interplay of two effects. Indeed, when NLO QCD corrections to top-quark decays are included ( $\text{NWA}_{\text{full}}$ ), the cross section receives negative corrections. On the other hand, when off-shell contributions are included, the correction to the cross section is positive.

With all the theoretical predictions available, we can check the importance of the full off-shell effects for the process, first at the integrated fiducial cross-section level, and in the next step differentially for various observables. As we have already mentioned the full off-shell predictions at NLO QCD accuracy consist of multiple effects. Firstly, they comprise the NLO QCD corrections not only to the production and decay stages of top quarks separately, but also radiative interference effects between the production and decay stage which represent genuine non-factorisable effects. Secondly, all heavy unstable particles are described by Breit-Wigner propagators in the matrix element calculations. Thirdly, they incorporate single- and non-resonant  $t$  and  $W^\pm/Z$  contributions. Finally, photon-induced contributions and  $Z/\gamma^*$  interference effects are included as well.

We start with the results for NLO integrated fiducial cross sections that are given in Table 7. For the default set of cuts we observe large effects. Specifically, the difference between the full off-shell result and  $\text{NWA}_{\text{full}}$  is of the order of 11%, which is well above the NWA uncertainty determined by

MODELLING	$\sigma_i^{\text{NLO}}$ [ab]	$\sigma_i^{\text{NLO}}/\sigma_{\text{NWA}_{\text{full}}}^{\text{NLO}} - 1$
Off-shell	98.88	+11.4 %
Off-shell $M_{\tau^+\tau^-}^{25 \text{ GeV}}$	91.00	+2.5 %
Off-shell $M_{\tau^+\tau^-}^{20 \text{ GeV}}$	89.96	+1.4 %
Off-shell $M_{\tau^+\tau^-}^{15 \text{ GeV}}$	88.44	-0.3 %
Off-shell $M_{\tau^+\tau^-}^{10 \text{ GeV}}$	85.74	-3.4 %
NWA <sub>full</sub>	88.75	-
NWA <sub>LOdec</sub>	96.74	+9.0 %

**Table 7.** *NLO integrated fiducial cross sections for the for  $pp \rightarrow e^+\nu_e \mu^-\bar{\nu}_\mu b\bar{b}\tau^+\tau^- + X$  at the LHC with  $\sqrt{s} = 13$  TeV. The full off-shell prediction and various NWA results are presented. Also given are the full off-shell findings with the additional  $|M_{\tau^+\tau^-} - m_Z| < X$  cut, where  $X \in \{25, 20, 15, 10\}$  GeV. The latter is denoted as  $M_{\tau^+\tau^-}^X$ . The NNPDF3.1 PDF sets are dynamical scale setting,  $\mu_R = \mu_F = \mu_0 = H_T/3$ , are used.*

$\mathcal{O}(\Gamma/m)$  for sufficiently inclusive processes [102]. The latter uncertainty for the  $pp \rightarrow t\bar{t}Z$  process with our rather inclusive setup is given by  $\mathcal{O}(\Gamma/m) \approx 2.7\%$ . When the additional  $|M_{\tau^+\tau^-} - m_Z| < X$  cut, where  $X \in \{25, 20, 15, 10\}$  GeV, is employed we can notice that full off-shell effects are substantially reduced and fall into the range 0.3% – 3.4% depending on the  $X$  value. Thus, this larger 11% effect is mostly driven by the  $Z/\gamma^*$  interference effects and photon-induced contributions. This is further confirmed by a previous study for the  $pp \rightarrow t\bar{t}Z$  process with  $Z \rightarrow \nu\bar{\nu}$ . Specifically, in Ref. [50] the final state  $pp \rightarrow e^+\nu_e \mu^-\bar{\nu}_\mu b\bar{b}\nu_\tau\bar{\nu}_\tau + X$  was considered with a fairly inclusive cut selection. For such a setup full off-shell effects of the order of 3% – 4% have been found, see Table 2 in Ref. [50].

To visualise this better we display in Figure 10 the NLO integrated fiducial cross section as a function of  $M_{\tau^+\tau^-}$ . The upper panel shows the absolute prediction at NLO for various approaches for the modelling of top-quark production and decays. Specifically, we show the full off-shell case without and with the  $|M_{\tau^+\tau^-} - m_Z| < 20$  (10) GeV cut. Also reported are the NWA<sub>full</sub> and NWA<sub>LOdec</sub> results. We additionally provide theoretical uncertainties as obtained from the scale dependence for the full off-shell case. The lower panel displays the ratios to the full off-shell prediction. We can observe that in the full off-shell case large tails from the Breit-Wigner  $Z$  propagator and the  $t\bar{t}Z/t\bar{t}\gamma^*$  interference are present. We can additionally notice substantial contributions from the  $t\bar{t}\gamma^*$  process for  $8 \text{ GeV} \lesssim M_{\tau^+\tau^-} \lesssim m_Z$ <sup>2</sup>. On the other hand, when the invariant mass of the  $\tau^+\tau^-$  system is set within a range of  $\pm 10$  GeV ( $\pm 20$  GeV) around the nominal  $Z$  boson mass we are more sensitive to on-shell-like  $Z$  boson decays. In these phase-space regions the photon-induced contribution as well as  $Z/\gamma^*$  interference effects are highly suppressed.

In the next step we analyse further various dimensionful observables. Specifically, in Figure 11 we show differential cross-section distributions as a function of  $p_{T b_1 b_2}$ ,  $p_{T b_1}$ ,  $M_{b\mu}^{\text{min}}$ ,  $p_{T \ell_2}$ ,  $p_{T \tau^+}$  and  $p_{T \tau^+\tau^-}$ . We focus on observables where the full off-shell effects are most pronounced. The latter are nevertheless visible for the majority of dimensionful differential cross sections. Very generally speaking the full off-shell effects are noticeable in the following two phase-space regions: in high  $p_T$  tails and in

<sup>2</sup>We note that the separation between the  $\tau^\pm$  leptons, implied by the  $\Delta R_{\tau^+\tau^-}$  cut, together with the requirement of having both  $\tau$  leptons with  $p_{T \tau} > 20$  GeV sets an effective lower limit on the invariant mass  $M_{\tau^+\tau^-}$ . Indeed, we can write  $(M_{\tau^+\tau^-})_{\text{min}} = (p_{T,\tau})_{\text{min}} \sqrt{2(1 - \cos(\Delta R_{\tau^+\tau^-}))} \approx 8$  GeV.

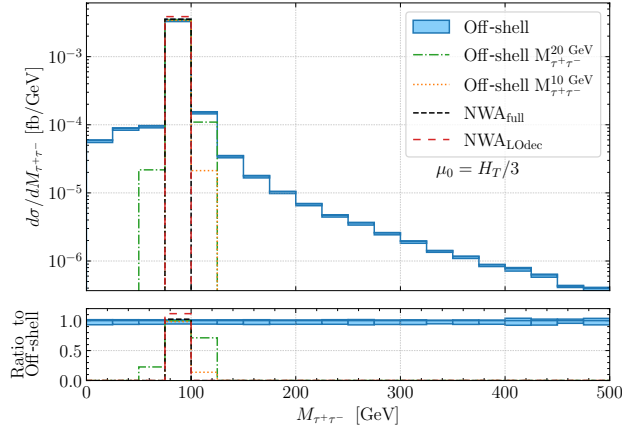


**Figure 10.** Differential cross-section distribution for  $pp \rightarrow e^+ \nu_e \mu^- \bar{\nu}_\mu b \bar{b} \tau^+ \tau^- + X$  at the LHC with  $\sqrt{s} = 13$  TeV as a function of  $M_{\tau^+\tau^-}$ . The upper panel shows the NLO QCD prediction for the full off-shell case as well as for  $\text{NWA}_{\text{full}}$  and  $\text{NWA}_{\text{LOdec}}$ . Also given is the full off-shell result with the additional  $|M_{\tau^+\tau^-} - m_Z| < 20$  (10) GeV cut. Furthermore, we provide theoretical uncertainties as obtained from the scale dependence for the full off-shell case. The lower panel displays the ratios to the full off-shell result. The scale choice is  $\mu_R = \mu_F = \mu_0 = H_T/3$ . The cross sections are evaluated with the NNPDF3.1 PDF set.

the vicinity of kinematical endpoints. In the following we shall provide examples for the both cases. The structure of each plot is the same as in Figure 10. Some of the observables displayed in Figure 11 have already been introduced. However, presented for the first time is the transverse momentum of the  $b\bar{b}$  system,  $p_{T_{b_1 b_2}}$ , the transverse momentum of the positively charged tau lepton,  $p_{T_{\tau^+}}$ , and the transverse momentum of the second hardest charged lepton,  $p_{T_{\ell_2}}$ , where  $\ell$  stands for  $\ell = e^+, \mu^-, \tau^+, \tau^-$ . Finally, also given is the minimum invariant mass of the  $b$ -jet and the muon,  $M_{b\mu^-}^{\text{min}}$ , which is defined as

$$M_{b\mu^-}^{\text{min}} = \min \{ M_{b_1\mu^-}, M_{b_2\mu^-} \}. \quad (6.4)$$

In the case when the top quarks and  $W$  gauge bosons are on-shell and the masses of all final decay products are neglected the  $M_{b\mu^-}^{\text{min}}$  observable is bounded from above by  $\sqrt{m_t^2 - m_W^2} \approx 153$  GeV. For the off-shell prediction this kinematic limit is smeared, nevertheless there is a sharp fall of the cross section for  $M_{b\mu^-}^{\text{min}} \gtrsim 153$  GeV. Even for the  $\text{NWA}_{\text{full}}$  and  $\text{NWA}_{\text{LOdec}}$  cases at NLO in QCD this endpoint is smeared by real emission contributions.

For the transverse momentum distribution of the  $b\bar{b}$  system we can detect substantial effects. Already for  $p_{T_{b_1 b_2}} \approx 400$  GeV the difference between the full off-shell result and the  $\text{NWA}_{\text{full}}$  prediction is about 30%. At the end of the plotted spectrum the full off-shell effects are even larger up to 40% – 45%. In spite of the fact that theoretical uncertainties due to the scale dependence are particularly large for this observable,  $\text{NWA}_{\text{full}}$  and  $\text{NWA}_{\text{LOdec}}$  are still outside of the uncertainty bands. The latter are at most at the 20% – 30% level in the aforementioned phase-space regions. If the additional  $|M_{\tau^+\tau^-} - m_Z| < 20$  (10) GeV cut is imposed the full off-shell effects are reduced to 15% – 20% for  $p_{T_{b_1 b_2}} \approx 400$  GeV, whereas they are up to 30% – 35% towards the end of the  $p_{T_{b_1 b_2}}$  spectrum. We can monitor the impact of higher-order corrections to top-quark decays by analysing the difference between  $\text{NWA}_{\text{full}}$  and  $\text{NWA}_{\text{LOdec}}$  predictions. We can see that NLO QCD corrections to top-quark decays are up to 10% – 13%, however, the shape distortions introduced by these higher order effects are larger and increase up to 23%.

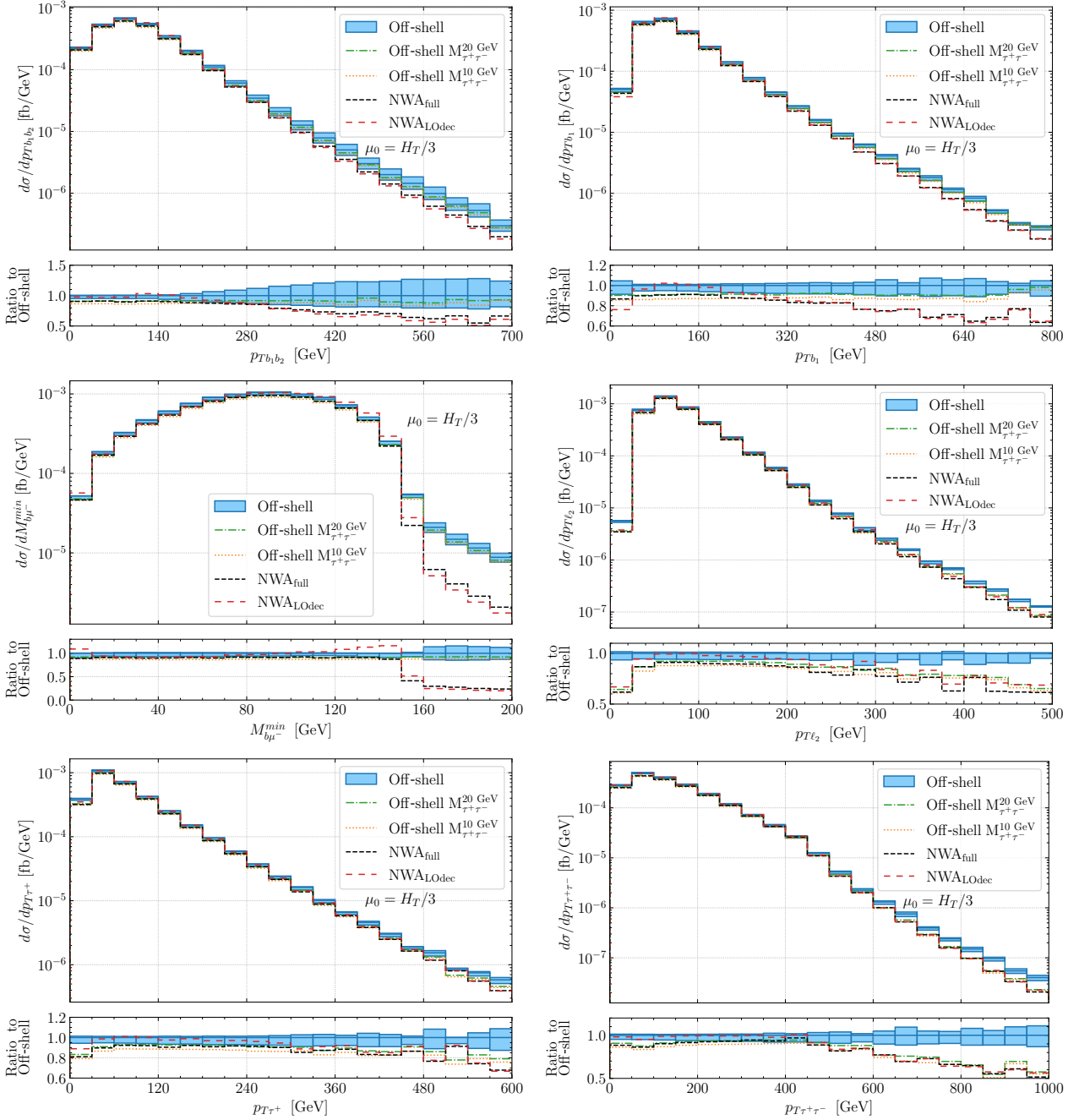


**Figure 11.** *Differential cross-section distributions for  $pp \rightarrow e^+ \nu_e \mu^- \bar{\nu}_\mu b \bar{b} \tau^+ \tau^- + X$  at the LHC with  $\sqrt{s} = 13$  TeV as a function of  $p_{T b \bar{b}}$ ,  $p_{T b_1}$ ,  $M_{b\mu}^{\min}$ ,  $p_{T \ell_2}$ ,  $p_{T \tau^+}$  and  $p_{T \tau^+ \tau^-}$ . The upper panel shows the NLO QCD prediction for the full off-shell case as well as for  $NWA_{\text{full}}$  and  $NWA_{\text{LOdec}}$ . Also given is the full off-shell result with the additional  $|M_{\tau^+ \tau^-} - m_Z| < 20$  (10) GeV cut. Furthermore, we provide theoretical uncertainties as obtained from the scale dependence for the full off-shell case. The lower panel displays the ratios to the full off-shell result. The scale choice is  $\mu_R = \mu_F = \mu_0 = H_T/3$ . The cross sections are evaluated with the NNPDF3.1 PDF set.*

For the transverse momentum of the hardest  $b$ -jet,  $p_{T b_1}$ , we can observe quite similar effects. The off-shell effects are up to 20% – 35% in  $p_T$  tails. Moreover, in the whole plotted range the  $NWA_{\text{full}}$  curve is outside of the uncertainty bands of the full off-shell result. NLO QCD corrections to top-quark

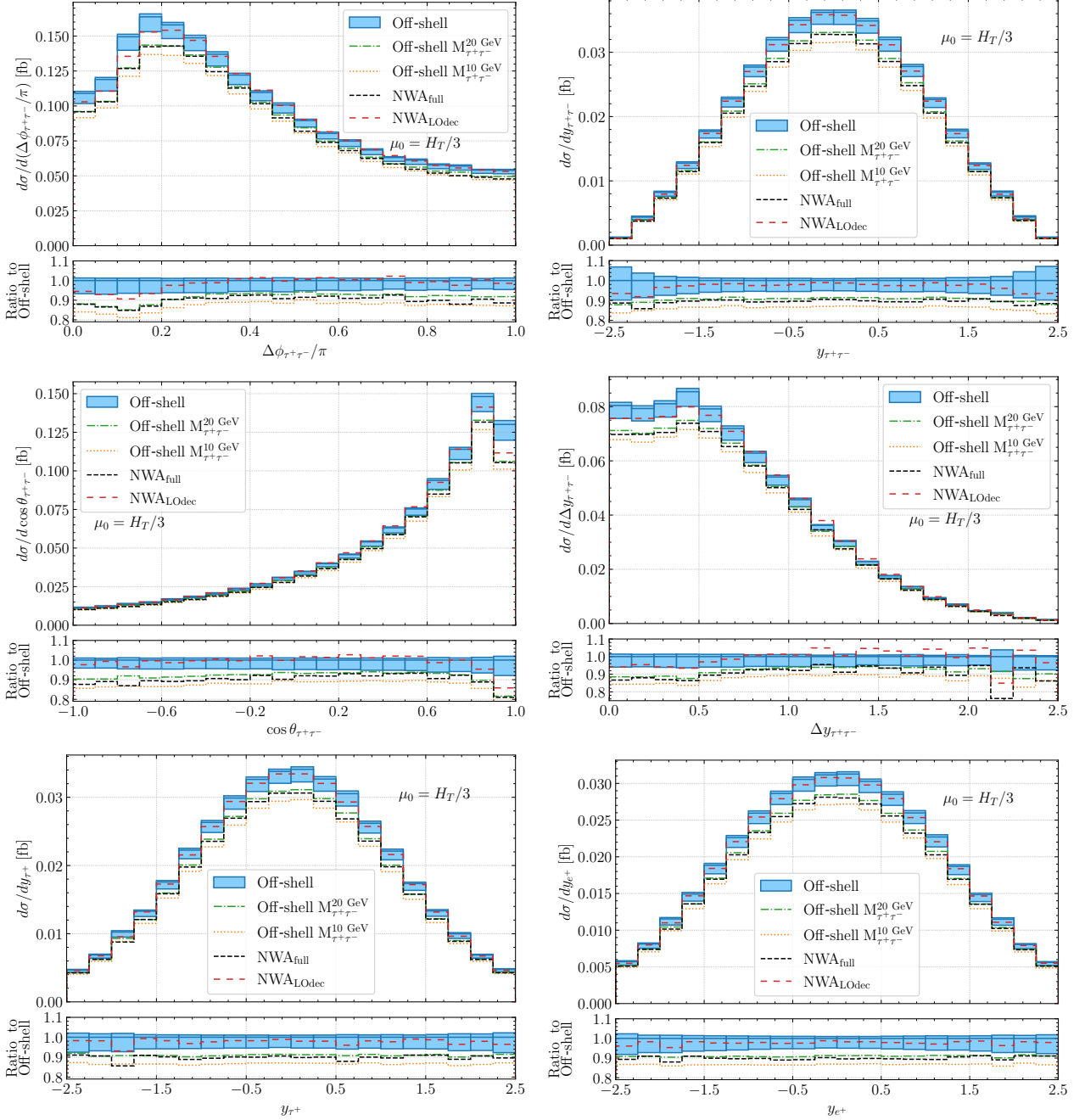


**Figure 12.** Differential cross-section distributions for  $pp \rightarrow e^+ \nu_e \mu^- \bar{\nu}_\mu b \bar{b} \tau^+ \tau^- + X$  at the LHC with  $\sqrt{s} = 13$  TeV as a function of  $\Delta\phi_{\tau^+\tau^-}$ ,  $y_{\tau^+\tau^-}$ ,  $\cos\theta_{\tau^+\tau^-}$ ,  $\Delta y_{\tau^+\tau^-}$ ,  $y_{\tau^+}$  and  $y_{e^+}$ . The upper panel shows the NLO QCD prediction for the full off-shell case as well as for  $\text{NWA}_{\text{full}}$  and  $\text{NWA}_{\text{LOdec}}$ . Also given is the full off-shell result with the additional  $|M_{\tau^+\tau^-} - m_Z| < 20$  (10) GeV cut. Furthermore, we provide theoretical uncertainties as obtained from the scale dependence for the full off-shell case. The lower panel displays the ratios to the full off-shell result. The scale choice is  $\mu_R = \mu_F = \mu_0 = H_T/3$ . The cross sections are evaluated with the NNPDF3.1 PDF set.

decays affect the distribution only for moderate  $p_{T b_1}$  values, i.e. up to about 300 GeV, and amount to 12% – 13%. They provide, however, the shape distortions up to 25%. The situation does not change significantly when the invariant mass of the two  $\tau$  leptons is restricted due to the extra cut.

We continue with differential cross section distributions as a function of the top-quark decay products and analyse in the next step the  $M_{b\mu^-}^{\min}$  observable. For the phase-space regions up to the kinematical endpoint, the relative difference between the full off-shell prediction and the  $\text{NWA}_{\text{full}}$  result is moderate and rather constant of the order of 10%. For  $M_{b\mu^-}^{\min} \approx 153$  GeV off-shell effects increase to about 60% whereas for  $M_{b\mu^-}^{\min} \approx 200$  GeV they are as high as 80%. For  $M_{b\mu^-}^{\min} \gtrsim 153$  GeV the  $\text{NWA}_{\text{full}}$  prediction simply fails to adequately describe this observable. This is not surprising since this kinematic range is dominated by a single-resonant top-quark contribution, which is missing from the  $\text{NWA}_{\text{full}}$  result. As for the NLO QCD corrections to top-quark decays we also observe a different behaviour in the two distinct phase-space regions, i.e. below and above the kinematic edge. For  $M_{b\mu^-}^{\min} < 153$  GeV higher-order effects are negative and in the range 1% – 30%. After reaching the kinematical limit of  $M_{b\mu^-}^{\min} \approx 153$  GeV they become positive and constant, of the order of 15%.

Next in line is the transverse momentum of the second hardest charged lepton,  $p_{T\ell_2}$ . In this case full off-shell effects are in the range of 10% – 40%. On the other hand, the scale dependence is only up to 10% in the whole plotted range. Higher-order effects in top-quark decay are negative and fairly constant at the level of 10%. As expected the additional  $M_{\tau^+\tau^-}$  cut has a sizable impact on the  $p_{T\ell_2}$  spectrum. This is due to the fact that  $p_{T\ell_2}$  comprises all charged leptons, thus, also  $\tau^+$  and  $\tau^-$  that are directly affected by this cut. Moreover, among the four charged leptons, the decay products of the  $Z$  boson have harder spectra than the leptons from the decays of top quarks. We can observe that the full off-shell prediction with the  $|M_{\tau^+\tau^-} - m_Z| < 10$  (20) GeV cut closely follows the  $\text{NWA}_{\text{full}}$  result. For the transverse momentum of the  $\tau^+$ ,  $p_{T\tau^+}$ , we observe qualitatively similar effects as for the  $p_{T\ell_2}$  observable.

The last observable plotted in Figure 11 is the transverse momentum of the  $\tau^+\tau^-$  system. Already at  $p_{T\tau^+\tau^-} \approx 600$  GeV full off-shell effects are at the level of 20%, and at the same time theoretical uncertainties are two times smaller. As we approach the end of the  $p_{T\tau^+\tau^-}$  spectrum the off-shell effects increase and are as high as 40% – 50%. Theoretical uncertainties though are only slightly higher there, i.e. they are at most 15%. Although NLO QCD corrections to top-quark decays are far from constant in the plotted range they reach maximally 10%. By employing the  $|M_{\tau^+\tau^-} - m_Z| < 10$  (20) GeV cut we essentially reproduce the on-shell prediction as given by the  $\text{NWA}_{\text{full}}$  curve.

Finally, in Figure 12 we display a few examples of dimensionless observables. In detail, we show differential cross-section distribution as a function of  $\Delta\phi_{\tau^+\tau^-}$ ,  $y_{\tau^+\tau^-}$ ,  $\cos\theta_{\tau^+\tau^-}$  and  $\Delta y_{\tau^+\tau^-}$ , where  $\Delta y_{\tau^+\tau^-} = |y_{\tau^+} - y_{\tau^-}|$ . Also given are rapidity distributions for  $\tau^+$ ,  $y_{\tau^+}$ , and for the positron,  $y_{e^+}$ . Dimensionless observables receive contributions from all phase-space regions, most notably from those that are sensitive to the threshold for the  $t\bar{t}Z$  production. Thus, the double-resonant top-quark and resonant  $Z$  gauge boson contributions have a dominant impact on these observables. Naively we would expect that the NWA should be good enough to properly describe the dimensionless observables. Yet, we can clearly observe that  $\text{NWA}_{\text{full}}$  fails to do this job for all the cases that we have presented. Indeed, the  $\text{NWA}_{\text{full}}$  curves are always outside of the uncertainty bands of the full off-shell results. These effects are even enhanced in the phase-space regions where the bulk of the cross section is located. Thus, photon-induced contributions and the  $Z/\gamma^*$  interference effects are very important also for angular distributions. We can further observe that the  $\text{NWA}_{\text{LOdec}}$  seems to correctly predict the dimensionless spectra in all phase-space regions. As already argued earlier in this Section, this agreement is accidental and cannot be understood as  $\text{NWA}_{\text{LOdec}}$  giving better predictions than those provided by  $\text{NWA}_{\text{full}}$ .

More specifically, for the  $\Delta\phi_{\tau^+\tau^-}/\pi$  observable full off-shell effects are up to 15% for the small values of  $\Delta\phi_{\tau^+\tau^-}/\pi$ , whereas for  $\Delta\phi_{\tau^+\tau^-}/\pi \approx 1$  they decrease to about 10%. Theoretical uncertainties due to the scale dependence are a factor of two smaller. Furthermore, we obtain negative NLO QCD

corrections to top-quark decays of the order of 10%.

For all rapidity distributions, i.e. for  $y_{\tau^+\tau^-}$ ,  $y_{\tau^+}$  and  $y_{e^+}$ , full off-shell effects and higher-order corrections to top-quark decays are alike. Both effects are rather constant and of the order of 10%. What makes them different is the sign of the effect. Also scale uncertainties are the same in all three cases. The latter are well below 10%. We add at this point that, also for the  $\Delta y_{\tau^+\tau^-} = |y_{\tau^+} - y_{\tau^-}|$  observable we observe qualitatively similar effects.

At last, in the case of  $\cos\theta_{\tau^+\tau^-}$  full off-shell effects are of the order of 10% in all but the last bin. In the latter the difference between  $\text{NWA}_{\text{full}}$  and the full off-shell prediction increases up to 20%. Theoretical uncertainties range respectively from about 5% up to maximally 8%. Also here, NLO QCD corrections to top-quark decays are negative and below 10%.

We conclude that for the observables that we have presented, which have been obtained with a rather inclusive set of cuts, the importance of a full off-shell calculation is rather clear. Not only high  $p_T$  tails and kinematical edges of dimensionful differential cross section distributions are poorly described by the NWA results but also angular distributions are affected. Thus even the latter would strongly benefit from the full off-shell predictions. Having such theoretical predictions at our disposal we can also analyse the impact of the additional  $|M_{\tau^+\tau^-} - m_Z| < 10$  (20) GeV cut on various observables. Namely, to understand the effect of enlarging or reducing the window of the invariant mass of the  $\tau^+\tau^-$  system around the nominal value of the mass of the  $Z$  gauge boson.

## 7 Summary

In this paper we calculated NLO QCD corrections to  $pp \rightarrow e^+\nu_e\mu^-\bar{\nu}_\mu b\bar{b}\tau^+\tau^- + X$  at the LHC with  $\sqrt{s} = 13$  TeV. In the computation off-shell top quarks and massive gauge bosons have been described by Breit-Wigner propagators, furthermore double-, single- and non-resonant top-quark contributions along with resonant and non-resonant  $Z$  as well as photon-induced contributions have been consistently incorporated already at the matrix element level. The total cross section and its scale dependence have been evaluated for two different scale choices, i.e. for the fixed scale  $\mu_R = \mu_F = \mu_0 = m_t + m_Z/2$  and for the dynamical one  $\mu_R = \mu_F = \mu_0 = H_T/3$ . The impact of the NLO QCD corrections on the integrated cross sections is moderate, of the order of 27% for  $\mu_0 = m_t + m_Z/2$  and 23% for  $\mu_0 = H_T/3$ . As to the theoretical uncertainty of our calculation, the contribution related to unknown higher-order corrections, as obtained by studying the scale dependence of our NLO predictions, is of the order of 6%. We have also analyzed the theoretical error arising from PDFs, being able to quantify it at the level of 1% for the default NNPDF3.1 PDF set. For other PDF sets, that we have examined, the PDF uncertainties are of the order of 2% – 3%. Thus, they are well below the uncertainty associated with the scale dependence.

For differential cross section distributions we have provided only predictions for the dynamical scale setting. The reason why we have not provided our results at the differential level for  $\mu_0 = m_t + m_Z/2$  is summarised in the following. Firstly, for the fixed scale choice we have noticed that for some choices of the scale the NLO results become negative. This happened in the high-energy tails of dimensionful distributions. Secondly, there are kinematic regions where the scale variation bands at LO and NLO do not overlap anymore. Thirdly, it has even happened that the scale variation at NLO has actually exceeded the scale variation of the LO predictions. All these effects have already been observed in our previous studies for  $t\bar{t}$  plus an additional object(s) and to a large extent have been accommodated by a judicious dynamical scale choice. In the case at hand for the dynamical scale setting, i.e. for  $\mu_0 = H_T/3$ , NLO QCD effects are up to 20%–50%. The theoretical uncertainties due to scale variations are, on the other hand, not higher than 10%. The latter are the dominant source of the theoretical

systematics since the NNPDF3.1 PDF uncertainties are very small and well below the corresponding theoretical uncertainties due to scale dependence.

We have additionally provided theoretical predictions for the  $t\bar{t}Z$  process in the tetra-lepton decay channel using the full NWA and the NWA with LO top-quark decays. We have noticed that the  $\text{NWA}_{\text{full}}$  prediction has the same theoretical uncertainties due to scale dependence as the full off-shell result. However, when higher-order corrections in top-quark decays are omitted, the scale dependence increases. For example, for the integrated fiducial cross section these theoretical uncertainties are at the level of 10%. Therefore, they are almost a factor of 2 larger than the theoretical uncertainty estimate for the  $\text{NWA}_{\text{full}}$  case. Furthermore, we have studied the impact of NLO QCD corrections to top-quark decays. These corrections are of the order of 10% for the integrated fiducial cross section. For various differential distributions the differences between the  $\text{NWA}_{\text{full}}$  and the  $\text{NWA}_{\text{LOdec}}$  case are of the same order. On top of that, having both theoretical predictions, full off-shell and  $\text{NWA}_{\text{full}}$  we have examined the impact of full off-shell effects at the integrated and differential fiducial level. For the integrated cross sections these effects are consistent with the expected accuracy of the NWA only when the  $|M_{\tau^+\tau^-} - m_Z| < X$  GeV cut, with  $X \in \{25, 20, 15, 10\}$  GeV, has been employed. Specifically, with this cut full off-shell effects are in the range 0.3% – 3.4%. Without this additional cut the full off-shell effects are as large as 11%. These large effects mostly originate from the photon-induced contributions and  $Z/\gamma^*$  interference effects. At the differential level, large non-factorisable corrections even up to 40% – 80% have been obtained for dimensionful differential cross sections. Poorly described by the  $\text{NWA}_{\text{full}}$  are also angular distributions. Thus, even the latter would strongly benefit from the full off-shell calculation.

In summary, the non-factorisable NLO QCD corrections impact significantly the  $t\bar{t}Z$  cross section in various phase-space regions. For this reason they should be included in future comparisons between theoretical predictions and experimental data. In addition, given the importance of the  $t\bar{t}Z$  process as background to Higgs boson production in association with a top-quark pair more detailed phenomenological studies in the tetra-lepton decay channel are required. We postpone such work for the future.

## Acknowledgments

The work of J.N. and M.W. was supported by the Deutsche Forschungsgemeinschaft (DFG) under grant 396021762 – TRR 257: *P3H - Particle Physics Phenomenology after the Higgs Discovery* and by the DFG under grant 400140256 - GRK 2497: *The physics of the heaviest particles at the Large Hardon Collider*.

Support by a grant of the Bundesministerium für Bildung und Forschung (BMBF) is additionally acknowledged.

The research of G.B. is supported by grant K 125105 of the National Research, Development and Innovation Office in Hungary.

The work of M.K. is supported in part by the U.S. Department of Energy under grant DE-SC0010102.

H.B.H. has received funding from the European Research Council (ERC) under the European Union’s Horizon 2020 Research and Innovation Programme (grant agreement no. 683211). Furthermore, the work of H.B.H has been partially supported by STFC consolidated HEP theory grant ST/T000694/1.

Simulations were performed with computing resources granted by RWTH Aachen University under projects `rwth0414` and `rwth0847`.

## References

- [1] CMS collaboration, *Measurement of the cross section for top quark pair production in association with a W or Z boson in proton-proton collisions at  $\sqrt{s} = 13$  TeV*, *JHEP* **08** (2018) 011 [[1711.02547](#)].
- [2] ATLAS collaboration, *Measurement of the  $t\bar{t}Z$  and  $t\bar{t}W$  cross sections in proton-proton collisions at  $\sqrt{s} = 13$  TeV with the ATLAS detector*, *Phys. Rev. D* **99** (2019) 072009 [[1901.03584](#)].
- [3] CMS collaboration, *Measurement of top quark pair production in association with a Z boson in proton-proton collisions at  $\sqrt{s} = 13$  TeV*, *JHEP* **03** (2020) 056 [[1907.11270](#)].
- [4] ATLAS collaboration, *Measurements of the inclusive and differential production cross sections of a top-quark-antiquark pair in association with a Z boson at  $\sqrt{s} = 13$  TeV with the ATLAS detector*, *Eur. Phys. J. C* **81** (2021) 737 [[2103.12603](#)].
- [5] N. Greiner, K. Kong, J.-C. Park, S. C. Park and J.-C. Winter, *Model-Independent Production of a Top-Philic Resonance at the LHC*, *JHEP* **04** (2015) 029 [[1410.6099](#)].
- [6] P. Cox, A. D. Medina, T. S. Ray and A. Spray, *Novel collider and dark matter phenomenology of a top-philic  $Z'$* , *JHEP* **06** (2016) 110 [[1512.00471](#)].
- [7] N. Kumar and S. P. Martin, *Vectorlike Leptons at the Large Hadron Collider*, *Phys. Rev. D* **92** (2015) 115018 [[1510.03456](#)].
- [8] J. H. Kim, K. Kong, S. J. Lee and G. Mohlabeng, *Probing TeV scale Top-Philic Resonances with Boosted Top-Tagging at the High Luminosity LHC*, *Phys. Rev. D* **94** (2016) 035023 [[1604.07421](#)].
- [9] P. J. Fox, I. Low and Y. Zhang, *Top-philic  $Z'$  forces at the LHC*, *JHEP* **03** (2018) 074 [[1801.03505](#)].
- [10] E. Alvarez, A. Juste, M. Szewc and T. Vazquez Schroeder, *Topping-up multilepton plus b-jets anomalies at the LHC with a  $Z'$  boson*, *JHEP* **05** (2021) 125 [[2011.06514](#)].
- [11] S. Bißmann, G. Hiller, C. Hormigos-Feliu and D. F. Litim, *Multi-lepton signatures of vector-like leptons with flavor*, *Eur. Phys. J. C* **81** (2021) 101 [[2011.12964](#)].
- [12] U. Baur, A. Juste, L. H. Orr and D. Rainwater, *Probing electroweak top quark couplings at hadron colliders*, *Phys. Rev. D* **71** (2005) 054013 [[hep-ph/0412021](#)].
- [13] U. Baur, A. Juste, D. Rainwater and L. H. Orr, *Improved measurement of  $ttZ$  couplings at the CERN LHC*, *Phys. Rev. D* **73** (2006) 034016 [[hep-ph/0512262](#)].
- [14] E. L. Berger, Q.-H. Cao and I. Low, *Model Independent Constraints Among the  $Wtb$ ,  $Zb$  anti- $b$ , and  $Zt$  anti- $t$  Couplings*, *Phys. Rev. D* **80** (2009) 074020 [[0907.2191](#)].
- [15] R. Röntsch and M. Schulze, *Constraining couplings of top quarks to the Z boson in  $t\bar{t} + Z$  production at the LHC*, *JHEP* **07** (2014) 091 [[1404.1005](#)].
- [16] R. Röntsch and M. Schulze, *Probing top-Z dipole moments at the LHC and ILC*, *JHEP* **08** (2015) 044 [[1501.05939](#)].
- [17] A. Buckley, C. Englert, J. Ferrando, D. J. Miller, L. Moore, M. Russell et al., *Constraining top quark effective theory in the LHC Run II era*, *JHEP* **04** (2016) 015 [[1512.03360](#)].
- [18] O. Bessidskaia Bylund, F. Maltoni, I. Tsirikos, E. Vryonidou and C. Zhang, *Probing top quark neutral couplings in the Standard Model Effective Field Theory at NLO in QCD*, *JHEP* **05** (2016) 052 [[1601.08193](#)].
- [19] M. Schulze and Y. Soreq, *Pinning down electroweak dipole operators of the top quark*, *Eur. Phys. J. C* **76** (2016) 466 [[1603.08911](#)].
- [20] N. P. Hartland, F. Maltoni, E. R. Nocera, J. Rojo, E. Slade, E. Vryonidou et al., *A Monte Carlo global analysis of the Standard Model Effective Field Theory: the top quark sector*, *JHEP* **04** (2019) 100 [[1901.05965](#)].

- [21] F. Maltoni, L. Mantani and K. Mimasu, *Top-quark electroweak interactions at high energy*, *JHEP* **10** (2019) 004 [[1904.05637](#)].
- [22] G. Durieux, A. Irlles, V. Miralles, A. Peñuelas, R. Pöschl, M. Perelló et al., *The electro-weak couplings of the top and bottom quarks — Global fit and future prospects*, *JHEP* **12** (2019) 98 [[1907.10619](#)].
- [23] I. Brivio, S. Bruggisser, F. Maltoni, R. Moutafis, T. Plehn, E. Vryonidou et al., *O new physics, where art thou? A global search in the top sector*, *JHEP* **02** (2020) 131 [[1910.03606](#)].
- [24] Y. Afik, S. Bar-Shalom, K. Pal, A. Soni and J. Wudka, *Multi-lepton probes of new physics and lepton-universality in top-quark interactions*, [2111.13711](#).
- [25] ATLAS collaboration, *Search for supersymmetry at  $\sqrt{s} = 13$  TeV in final states with jets and two same-sign leptons or three leptons with the ATLAS detector*, *Eur. Phys. J. C* **76** (2016) 259 [[1602.09058](#)].
- [26] CMS collaboration, *Search for new physics in same-sign dilepton events in proton–proton collisions at  $\sqrt{s} = 13$  TeV*, *Eur. Phys. J. C* **76** (2016) 439 [[1605.03171](#)].
- [27] ATLAS collaboration, *Search for supersymmetry in final states with two same-sign or three leptons and jets using  $36\text{ fb}^{-1}$  of  $\sqrt{s} = 13$  TeV pp collision data with the ATLAS detector*, *JHEP* **09** (2017) 084 [[1706.03731](#)].
- [28] CMS collaboration, *Search for physics beyond the standard model in events with two leptons of same sign, missing transverse momentum, and jets in proton–proton collisions at  $\sqrt{s} = 13$  TeV*, *Eur. Phys. J. C* **77** (2017) 578 [[1704.07323](#)].
- [29] ATLAS collaboration, *Search for squarks and gluinos in final states with same-sign leptons and jets using  $139\text{ fb}^{-1}$  of data collected with the ATLAS detector*, *JHEP* **06** (2020) 046 [[1909.08457](#)].
- [30] CMS collaboration, *Search for physics beyond the standard model in events with jets and two same-sign or at least three charged leptons in proton-proton collisions at  $\sqrt{s} = 13$  TeV*, *Eur. Phys. J. C* **80** (2020) 752 [[2001.10086](#)].
- [31] ATLAS collaboration, *Evidence for the associated production of the Higgs boson and a top quark pair with the ATLAS detector*, *Phys. Rev. D* **97** (2018) 072003 [[1712.08891](#)].
- [32] ATLAS COLLABORATION collaboration, *Analysis of  $t\bar{t}H$  and  $t\bar{t}W$  production in multilepton final states with the ATLAS detector*, tech. rep., CERN, Geneva, Oct, 2019.
- [33] CMS collaboration, *Measurement of the Higgs boson production rate in association with top quarks in final states with electrons, muons, and hadronically decaying tau leptons at  $\sqrt{s} = 13$  TeV*, *Eur. Phys. J. C* **81** (2021) 378 [[2011.03652](#)].
- [34] ATLAS collaboration, *Observation of the associated production of a top quark and a Z boson in pp collisions at  $\sqrt{s} = 13$  TeV with the ATLAS detector*, *JHEP* **07** (2020) 124 [[2002.07546](#)].
- [35] CMS collaboration, *Inclusive and differential cross section measurements of single top quark production in association with a Z boson in proton-proton collisions at  $\sqrt{s} = 13$  TeV*, [2111.02860](#).
- [36] A. Lazopoulos, T. McElmurry, K. Melnikov and F. Petriello, *Next-to-leading order QCD corrections to  $t\bar{t}Z$  production at the LHC*, *Phys. Lett. B* **666** (2008) 62 [[0804.2220](#)].
- [37] A. Kardos, Z. Trocsanyi and C. Papadopoulos, *Top quark pair production in association with a Z-boson at NLO accuracy*, *Phys. Rev. D* **85** (2012) 054015 [[1111.0610](#)].
- [38] F. Maltoni, D. Pagani and I. Tsirikos, *Associated production of a top-quark pair with vector bosons at NLO in QCD: impact on  $t\bar{t}H$  searches at the LHC*, *JHEP* **02** (2016) 113 [[1507.05640](#)].
- [39] S. Frixione, V. Hirschi, D. Pagani, H. S. Shao and M. Zaro, *Electroweak and QCD corrections to top-pair hadroproduction in association with heavy bosons*, *JHEP* **06** (2015) 184 [[1504.03446](#)].
- [40] A. Broggio, A. Ferroglia, G. Ossola, B. D. Pecjak and R. D. Sameshima, *Associated production of a top pair and a Z boson at the LHC to NNLL accuracy*, *JHEP* **04** (2017) 105 [[1702.00800](#)].

- [41] A. Kulesza, L. Motyka, D. Schwartländer, T. Stebel and V. Theeuwes, *Associated production of a top quark pair with a heavy electroweak gauge boson at NLO+NNLL accuracy*, *Eur. Phys. J. C* **79** (2019) 249 [[1812.08622](#)].
- [42] A. Broggio, A. Ferroglia, R. Frederix, D. Pagani, B. D. Pecjak and I. Tsinikos, *Top-quark pair hadroproduction in association with a heavy boson at NLO+NNLL including EW corrections*, *JHEP* **08** (2019) 039 [[1907.04343](#)].
- [43] A. Kulesza, L. Motyka, D. Schwartländer, T. Stebel and V. Theeuwes, *Associated top quark pair production with a heavy boson: differential cross sections at NLO+NNLL accuracy*, *Eur. Phys. J. C* **80** (2020) 428 [[2001.03031](#)].
- [44] M. V. Garzelli, A. Kardos, C. G. Papadopoulos and Z. Trocsanyi,  *$Z^0$  - boson production in association with a top anti-top pair at NLO accuracy with parton shower effects*, *Phys. Rev. D* **85** (2012) 074022 [[1111.1444](#)].
- [45] M. V. Garzelli, A. Kardos, C. G. Papadopoulos and Z. Trocsanyi,  *$t\bar{t}W^\pm$  and  $t\bar{t}Z$  Hadroproduction at NLO accuracy in QCD with Parton Shower and Hadronization effects*, *JHEP* **11** (2012) 056 [[1208.2665](#)].
- [46] M. Ghezzi, B. Jager, S. L. P. Chavez, L. Reina and D. Wackerroth, *Hadronic production of top-quark pairs in association with a pair of leptons in the POWHEG BOX framework*, [2112.08892](#).
- [47] S. Frixione, E. Laenen, P. Motylinski and B. R. Webber, *Angular correlations of lepton pairs from vector boson and top quark decays in Monte Carlo simulations*, *JHEP* **04** (2007) 081 [[hep-ph/0702198](#)].
- [48] G. Altarelli, L. Conti and V. Lubicz, *The  $t \rightarrow WZb$  decay in the standard model: A Critical reanalysis*, *Phys. Lett. B* **502** (2001) 125 [[hep-ph/0010090](#)].
- [49] G. Bevilacqua, H. B. Hartanto, M. Kraus, T. Weber and M. Worek, *Towards constraining Dark Matter at the LHC: Higher order QCD predictions for  $t\bar{t} + Z(Z \rightarrow \nu_e \bar{\nu}_e)$* , *JHEP* **11** (2019) 001 [[1907.09359](#)].
- [50] J. Hermann and M. Worek, *The impact of top-quark modelling on the exclusion limits in  $t\bar{t} + DM$  searches at the LHC*, *Eur. Phys. J. C* **81** (2021) 1029 [[2108.01089](#)].
- [51] R. V. Harlander, S. Y. Klein and M. Lipp, *FeynGame*, *Comput. Phys. Commun.* **256** (2020) 107465 [[2003.00896](#)].
- [52] M. Czakon, C. G. Papadopoulos and M. Worek, *Polarizing the Dipoles*, *JHEP* **08** (2009) 085 [[0905.0883](#)].
- [53] A. Cafarella, C. G. Papadopoulos and M. Worek, *Helac-Phegas: A Generator for all parton level processes*, *Comput. Phys. Commun.* **180** (2009) 1941 [[0710.2427](#)].
- [54] P. Draggiotis, R. H. P. Kleiss and C. G. Papadopoulos, *On the computation of multigluon amplitudes*, *Phys. Lett. B* **439** (1998) 157 [[hep-ph/9807207](#)].
- [55] A. Kanaki and C. G. Papadopoulos, *HELAC: A Package to compute electroweak helicity amplitudes*, *Comput. Phys. Commun.* **132** (2000) 306 [[hep-ph/0002082](#)].
- [56] P. D. Draggiotis, R. H. P. Kleiss and C. G. Papadopoulos, *Multijet production in hadron collisions*, *Eur. Phys. J. C* **24** (2002) 447 [[hep-ph/0202201](#)].
- [57] A. van Hameren, *PARNI for importance sampling and density estimation*, *Acta Phys. Polon. B* **40** (2009) 259 [[0710.2448](#)].
- [58] A. van Hameren, *Kaleu: A General-Purpose Parton-Level Phase Space Generator*, [1003.4953](#).
- [59] C. G. Papadopoulos, *PHEGAS: A Phase space generator for automatic cross-section computation*, *Comput. Phys. Commun.* **137** (2001) 247 [[hep-ph/0007335](#)].
- [60] A. Denner, S. Dittmaier, M. Roth and D. Wackerroth, *Predictions for all processes  $e^+e^- \rightarrow 4$  fermions +  $\gamma$* , *Nucl. Phys. B* **560** (1999) 33 [[hep-ph/9904472](#)].

- [61] A. Denner, S. Dittmaier, M. Roth and L. H. Wieders, *Electroweak corrections to charged-current  $e^+e^- \rightarrow 4$  fermion processes: Technical details and further results*, *Nucl. Phys. B* **724** (2005) 247 [[hep-ph/0505042](#)].
- [62] P. Nogueira, *Automatic Feynman graph generation*, *J. Comput. Phys.* **105** (1993) 279.
- [63] A. van Hameren, C. G. Papadopoulos and R. Pittau, *Automated one-loop calculations: A Proof of concept*, *JHEP* **09** (2009) 106 [[0903.4665](#)].
- [64] G. Ossola, C. G. Papadopoulos and R. Pittau, *Reducing full one-loop amplitudes to scalar integrals at the integrand level*, *Nucl. Phys. B* **763** (2007) 147 [[hep-ph/0609007](#)].
- [65] G. Ossola, C. G. Papadopoulos and R. Pittau, *CutTools: A Program implementing the OPP reduction method to compute one-loop amplitudes*, *JHEP* **03** (2008) 042 [[0711.3596](#)].
- [66] G. Ossola, C. G. Papadopoulos and R. Pittau, *On the Rational Terms of the one-loop amplitudes*, *JHEP* **05** (2008) 004 [[0802.1876](#)].
- [67] P. Draggiotis, M. V. Garzelli, C. G. Papadopoulos and R. Pittau, *Feynman Rules for the Rational Part of the QCD 1-loop amplitudes*, *JHEP* **04** (2009) 072 [[0903.0356](#)].
- [68] A. van Hameren, *OneLOop: For the evaluation of one-loop scalar functions*, *Comput. Phys. Commun.* **182** (2011) 2427 [[1007.4716](#)].
- [69] J. Alwall, R. Frederix, S. Frixione, V. Hirschi, F. Maltoni, O. Mattelaer et al., *The automated computation of tree-level and next-to-leading order differential cross sections, and their matching to parton shower simulations*, *JHEP* **07** (2014) 079 [[1405.0301](#)].
- [70] S. Badger, B. Biedermann and P. Uwer, *NGluon: A Package to Calculate One-loop Multi-gluon Amplitudes*, *Comput. Phys. Commun.* **182** (2011) 1674 [[1011.2900](#)].
- [71] S. Catani and M. H. Seymour, *A General algorithm for calculating jet cross-sections in NLO QCD*, *Nucl. Phys. B* **485** (1997) 291 [[hep-ph/9605323](#)].
- [72] S. Catani, S. Dittmaier, M. H. Seymour and Z. Trocsanyi, *The Dipole formalism for next-to-leading order QCD calculations with massive partons*, *Nucl. Phys. B* **627** (2002) 189 [[hep-ph/0201036](#)].
- [73] G. Bevilacqua, M. Czakon, M. Kubocz and M. Worek, *Complete Nagy-Soper subtraction for next-to-leading order calculations in QCD*, *JHEP* **10** (2013) 204 [[1308.5605](#)].
- [74] Z. Nagy and Z. Trocsanyi, *Next-to-leading order calculation of four jet observables in electron positron annihilation*, *Phys. Rev. D* **59** (1999) 014020 [[hep-ph/9806317](#)].
- [75] Z. Nagy, *Next-to-leading order calculation of three jet observables in hadron hadron collision*, *Phys. Rev. D* **68** (2003) 094002 [[hep-ph/0307268](#)].
- [76] G. Bevilacqua, M. Czakon, C. G. Papadopoulos, R. Pittau and M. Worek, *Assault on the NLO Wishlist:  $pp \rightarrow t\bar{t}b\bar{b}$* , *JHEP* **09** (2009) 109 [[0907.4723](#)].
- [77] M. Czakon, H. B. Hartanto, M. Kraus and M. Worek, *Matching the Nagy-Soper parton shower at next-to-leading order*, *JHEP* **06** (2015) 033 [[1502.00925](#)].
- [78] G. Bevilacqua, M. Czakon, M. V. Garzelli, A. van Hameren, A. Kardos, C. G. Papadopoulos et al., *HELAC-NLO*, *Comput. Phys. Commun.* **184** (2013) 986 [[1110.1499](#)].
- [79] J. Alwall et al., *A Standard format for Les Houches event files*, *Comput. Phys. Commun.* **176** (2007) 300 [[hep-ph/0609017](#)].
- [80] I. Antcheva et al., *ROOT: A C++ framework for petabyte data storage, statistical analysis and visualization*, *Comput. Phys. Commun.* **180** (2009) 2499 [[1508.07749](#)].
- [81] Z. Bern, L. J. Dixon, F. Febres Cordero, S. Höche, H. Ita, D. A. Kosower et al., *Ntuples for NLO Events at Hadron Colliders*, *Comput. Phys. Commun.* **185** (2014) 1443 [[1310.7439](#)].

- [82] M. Jezabek and J. H. Kuhn, *QCD Corrections to Semileptonic Decays of Heavy Quarks*, *Nucl. Phys. B* **314** (1989) 1.
- [83] L. Basso, S. Dittmaier, A. Huss and L. Oggero, *Techniques for the treatment of IR divergences in decay processes at NLO and application to the top-quark decay*, *Eur. Phys. J. C* **76** (2016) 56 [[1507.04676](#)].
- [84] M. Cacciari, G. P. Salam and G. Soyez, *The anti- $k_t$  jet clustering algorithm*, *JHEP* **04** (2008) 063 [[0802.1189](#)].
- [85] J. Butterworth et al., *PDF4LHC recommendations for LHC Run II*, *J. Phys. G* **43** (2016) 023001 [[1510.03865](#)].
- [86] NNPDF collaboration, *Parton distributions from high-precision collider data*, *Eur. Phys. J. C* **77** (2017) 663 [[1706.00428](#)].
- [87] A. Buckley, J. Ferrando, S. Lloyd, K. Nordström, B. Page, M. Rüfenacht et al., *LHAPDF6: parton density access in the LHC precision era*, *Eur. Phys. J. C* **75** (2015) 132 [[1412.7420](#)].
- [88] H.-L. Lai, M. Guzzi, J. Huston, Z. Li, P. M. Nadolsky, J. Pumplin et al., *New parton distributions for collider physics*, *Phys. Rev. D* **82** (2010) 074024 [[1007.2241](#)].
- [89] S. Dulat, T.-J. Hou, J. Gao, M. Guzzi, J. Huston, P. Nadolsky et al., *New parton distribution functions from a global analysis of quantum chromodynamics*, *Phys. Rev. D* **93** (2016) 033006 [[1506.07443](#)].
- [90] T.-J. Hou et al., *New CTEQ global analysis of quantum chromodynamics with high-precision data from the LHC*, *Phys. Rev. D* **103** (2021) 014013 [[1912.10053](#)].
- [91] A. D. Martin, W. J. Stirling, R. S. Thorne and G. Watt, *Parton distributions for the LHC*, *Eur. Phys. J. C* **63** (2009) 189 [[0901.0002](#)].
- [92] L. Harland-Lang, A. Martin, P. Motylinski and R. Thorne, *Parton distributions in the LHC era: MMHT 2014 PDFs*, *Eur. Phys. J. C* **75** (2015) 204 [[1412.3989](#)].
- [93] S. Bailey, T. Cridge, L. A. Harland-Lang, A. D. Martin and R. S. Thorne, *Parton distributions from LHC, HERA, Tevatron and fixed target data: MSHT20 PDFs*, *Eur. Phys. J. C* **81** (2021) 341 [[2012.04684](#)].
- [94] NNPDF collaboration, *Parton distributions for the LHC Run II*, *JHEP* **04** (2015) 040 [[1410.8849](#)].
- [95] R. D. Ball et al., *The Path to Proton Structure at One-Percent Accuracy*, [2109.02653](#).
- [96] S. Alekhin, J. Blümlein and S. Moch, *NLO PDFs from the ABMP16 fit*, *Eur. Phys. J. C* **78** (2018) 477 [[1803.07537](#)].
- [97] G. Bevilacqua, H. B. Hartanto, M. Kraus and M. Worek, *Off-shell Top Quarks with One Jet at the LHC: A comprehensive analysis at NLO QCD*, *JHEP* **11** (2016) 098 [[1609.01659](#)].
- [98] G. Bevilacqua, H. B. Hartanto, M. Kraus, T. Weber and M. Worek, *Hard Photons in Hadroproduction of Top Quarks with Realistic Final States*, *JHEP* **10** (2018) 158 [[1803.09916](#)].
- [99] G. Bevilacqua, H.-Y. Bi, H. B. Hartanto, M. Kraus and M. Worek, *The simplest of them all:  $t\bar{t}W^\pm$  at NLO accuracy in QCD*, *JHEP* **08** (2020) 043 [[2005.09427](#)].
- [100] D. Stremmer and M. Worek, *Production and decay of the Higgs boson in association with top quarks*, [2111.01427](#).
- [101] G. Bevilacqua, H. B. Hartanto, M. Kraus, T. Weber and M. Worek, *Off-shell vs on-shell modelling of top quarks in photon associated production*, *JHEP* **03** (2020) 154 [[1912.09999](#)].
- [102] V. S. Fadin, V. A. Khoze and A. D. Martin, *How suppressed are the radiative interference effects in heavy instable particle production?*, *Phys. Lett. B* **320** (1994) 141 [[hep-ph/9309234](#)].